



# A Technique to Measure Coronal Electron Density, Temperature, and Velocity Above $2.5 R_{\odot}$ from Sun Center Using Polarized Brightness Spectrum

Nelson Reginald<sup>1,2</sup> · Jeffrey Newmark<sup>2</sup> · Lutz Rastaetter<sup>3</sup>

Received: 20 December 2022 / Accepted: 22 April 2023  
© The Author(s), under exclusive licence to Springer Nature B.V. 2023

## Abstract

The current model for the polarized brightness (pB) spectrum has a decades-long history of progressively incorporating its dependence on electron density  $N_e$ , temperature  $T_e$ , and flow velocity in the radial direction  $V_e$ . The  $pB_{N_e}$  spectrum follows the exact shape of the photosphere spectrum, which is not smooth, which is expected from the thermal Doppler broadening of the photosphere spectrum due to the high coronal  $T_e$ ; the  $pB_{N_e T_e}$  spectrum is smooth, but the free coronal electrons remain static and unaffected by solar wind, and the  $pB_{N_e T_e V_e}$  spectrum is red-shifted by electrons seeing a red-shifted photosphere spectrum as they flow away from the Sun as solar wind, which takes a radial direction above  $2.5 R_{\odot}$  from Sun center. In this article, we review the progress of the above three model pB spectra in describing the observations and highlight the differences, first by comparing the three model pB spectra against wavelength using a model for  $N_e$  and constant values for  $T_e$  and  $V_e$ , and second by generating three model 2D pB maps by integrating over a selected wavelength region in the three model pB spectra along lines of sight passing through the 14 July 2000 (“Bastille Day”) coronal mass ejection (CME) model, which contains 3D information on  $N_e$ ,  $T_e$ , and  $V_e$ . In this regard, the *CORONAL Diagnostic EXperiment* (CODEX) on the *International Space Station* (ISS) in 2024 will measure  $N_e$ ,  $T_e$ , and  $V_e$  by matching the measured pB with modeled  $pB_{N_e T_e V_e}$  in selected wavelength regions using multiple filters.

**Keywords** Electron density · Electron temperature · Electron velocity

---

✉ N. Reginald  
[Nelson.L.Reginald@nasa.gov](mailto:Nelson.L.Reginald@nasa.gov)

J. Newmark  
[Jeffrey.Newmark@nasa.gov](mailto:Jeffrey.Newmark@nasa.gov)

L. Rastaetter  
[Lutz.Rastaetter-1@nasa.gov](mailto:Lutz.Rastaetter-1@nasa.gov)

<sup>1</sup> Department of Physics, The Catholic University of America, 620 Michigan Avenue NE, Washington, D.C., 20064, USA

<sup>2</sup> MC 671, NASA Goddard Space Flight Center, Greenbelt, MD 20771, USA

<sup>3</sup> MC 674, NASA Goddard Space Flight Center, Greenbelt, MD 20771, USA

## 1. Introduction

The *kontinuierliche*, for continuum, (K) corona brightness spectrum is the photospheric spectrum Thomson scattered off free coronal electrons. The sum  $[I^T + I^R]$  of its tangential  $[I^T]$  and radial  $[I^R]$  polarized components is the total K-corona brightness (TB) spectrum, whereas the difference  $[I^T - I^R]$  is the polarized K-corona brightness (pB) spectrum. Thomson scattering is elastic, which means that the energy and wavelength of the photon incident on the electron are preserved upon scattering. Thomson scattering can also happen off coronal protons, but the associated brightness is negligible compared to the electrons. This is because the proton is  $\approx 1840$  times heavier than the electron and the Thomson-scattering cross section is inversely proportional to the square of the mass. Measuring pB using better and better space- and ground-based coronagraphic techniques and modeling pB for better and better matching with measured pB plays a very important role in the study of the solar corona. With pB spread nonuniformly throughout the hot and dynamic solar coronal environment using pB to measure electron parameters such as electron density  $[N_e]$ , temperature  $[T_e]$ , and bulk, flow velocity (or solar-wind velocity)  $[V_e]$  in the radial direction, which becomes important above  $2.5 R_\odot$  from Sun center, can be used to check how well they complement similar measurements for protons and provide additional insight into solving mysteries of the solar corona, such as the origins of the  $T_e$  measured in mega-Kelvins and acceleration of  $V_e$  to reach the escape velocity of the Sun and allow the solar wind to reach the Earth.

Measuring pB traditionally involved taking three consecutive images of the solar corona,  $I_{0^\circ}$ ,  $I_{120^\circ}$ , and  $I_{240^\circ}$ , through a linear polarizer by turning the linear polarizer in intervals of  $120^\circ$ , which is explained in detail by Billings (1966) and ubiquitously used by ground- and space-based white-light coronagraphs. Examples of spacecraft-based coronagraphs that implement this technique are the *Coronagraph 1* (COR1) and *Coronagraph 2* (COR2) instruments onboard the *Solar Terrestrial Relations Observatory* (STEREO) spacecraft (see Howard et al., 2008) and *Large Angle Spectrometric CORonagraph* (LASCO) *Coronagraph 1* (C1 with a tunable Fabry–Pérot interferometer narrow bandpass spectral filter system), *Coronagraph 2* (C2), and *Coronagraph 3* (C3) instruments onboard the *Solar and Heliospheric Observatory* (SOHO) spacecraft (see Brueckner et al., 1995). Another technique to measure pB is by taking four consecutive images  $[I_{0^\circ}, I_{45^\circ}, I_{90^\circ}, \text{ and } I_{135^\circ}]$  by turning the linear polarizer in intervals of  $45^\circ$ , which is also explained in detail by Billings (1966), or by taking four simultaneous images  $[I_{0^\circ}, I_{45^\circ}, I_{90^\circ}, \text{ and } I_{135^\circ}]$  using a polarization camera, where the four orientations of the linear polarizer are permanently embedded on the detector, which is explained in detail by Reginald et al. (2017). In Section 2, we present a summary on how the three and four coronal image sets  $[I_{0^\circ}, I_{120^\circ}, I_{240^\circ}]$  and  $[I_{0^\circ}, I_{45^\circ}, I_{90^\circ}, I_{135^\circ}]$ , respectively, can be manipulated to measure  $(I^T - I^R)$ : pB.

Modeling pB has evolved over many decades by progressively incorporating the influence of  $N_e$ ,  $T_e$ , and  $V_e$ . In summary, van de Hulst (1950) presented a theoretical model for the pB spectrum, which was dependent on  $N_e$ , that followed the shape of the photospheric spectrum but lacked the expected smoothness due to electrons vibrating from high  $T_e$  measured in mega-Kelvins and thermal Doppler broadening the photosphere spectrum. We call this model  $\text{pB}_{N_e}$ . Two decades later, Cram (1976) presented a theoretical model for the pB spectrum, which was dependent on both  $N_e$  and  $T_e$  and accounted for the expected smoothness of the pB spectrum, but lacked the expected red-shifting of the pB spectrum due to the radial flow of electrons away from the Sun as solar wind, which materializes around  $2.5 R_\odot$  from Sun center, and in the process seeing a red-shifted photosphere spectrum. We call this model  $\text{pB}_{N_e T_e}$ . Two decades later, Reginald (2001) presented a theoretical model for the pB

spectrum, which was dependent on  $N_e$ ,  $T_e$ , and  $V_e$  and accounted for the red-shifting of the pB spectrum. We call this model  $pB_{N_e T_e V_e}$ . In this article, we review the expressions for the three model pB spectra,  $pB_{N_e}$  in Section 3.1,  $pB_{N_e T_e}$  in Section 3.2, and  $pB_{N_e T_e V_e}$  in Section 3.3, and highlight any differences using plots of the three model pB spectra as functions of wavelength from 370.0 nm to 470.0 nm. In Section 4, we plot three model 2D pB maps associated with the three model pB spectra by integrating over select wavelength regions along lines of sight passing through the 14 July 2000 (“Bastille Day”) coronal mass ejection (CME) model, which contains 3D information on  $N_e$ ,  $T_e$ , and  $V_e$  to highlight differences on a global scale.

The purpose of this article is to compile from the literature a list of popular techniques used in measuring pB and present the historical progression on modeling pB to reach the current state for the purpose of introducing the *CO*ronal *D*iagnostic *EX*periment (CODEX) instrument. CODEX will measure pB through multiple color filters and a polarization camera and then interpret them in terms of  $N_e$ ,  $T_e$ , and  $V_e$  in the radial direction using  $pB_{N_e T_e V_e}$ . CODEX is currently being assembled at the National Aeronautics and Space Administration (NASA) – Goddard Space Flight Center (GSFC) in equal partnership with the Korea Astronomy and Space Science Institute (KASI) and is scheduled to fly to the *International Space Station* (ISS) in 2024. In CODEX, two pairs of color filters centered at (393.5, 405.0) nm and (398.7, 423.3) nm, and each with a bandwidth of 10.0 nm will be used to measure two pB ratios, which we call the Temperature Sensitive Brightness Ratio (TSBR) to measure  $T_e$  and the Speed Sensitive Brightness Ratio (SSBR) to measure  $V_e$  in the radial direction, respectively, by comparing with modeled TSBR and SSBR, respectively. The pB measured through the four filters will be used for four independent measurements of  $N_e$ . For simplicity, we say that CODEX uses a Filter Ratio Technique (FRT). Since the intent of this article is not about describing CODEX but emphasizing the underlying properties of pB exploited by CODEX, we limit ourselves to only mentioning three articles related to FRT: i) Reginald, Newmark, and Rastaetter (2021) present modeling FRT to quantify the statistical error due to both polarized and unpolarized sources of brightness illuminating a polarization camera and its effects on the measurements of  $T_e$  and  $V_e$ ; ii) Reginald et al. (2018) present a synthetic FRT experiment to quantify systematic error on the measurements of  $T_e$  and  $V_e$  from using modeled TSBR and SSBR based on symmetric coronal models to interpret measured TSBR and SSBR in an asymmetric corona; iii) Reginald, Newmark, and Rastaetter (2020) show how to correct the systematic error in FRT or use uncorrected FRT as an additional tool for space-weather prediction. A convenient unit used in all three articles is to quantify pB in units of spectral radiance given by  $J s^{-1} m^{-2} \Omega^{-1} nm^{-1}$ . To be consistent, we will use the same units for modeling pB. Note that we use  $J s^{-1}$  rather than Watts.

To model pB requires a photospheric spectrum to Thomson scatter off the free coronal electrons. The photosphere spectrum used in this article is shown in Figure 1 in units of solar spectral radiance (SSR) given by  $J s^{-1} m^{-2} \Omega^{-1} nm^{-1}$  as a function of wavelength expressed in nm. The SSR from Kurucz et al. (1984) was measured using a ground-based Fourier transform spectroscope located at the McMath–Pierce Solar Telescope at Kitt Peak, Arizona, USA, and corrected for wavelength-dependent absorption by the Earth’s atmosphere. Note: The same photospheric spectrum shown in Figure 1 was used in the three articles related to FRT. When the real CODEX experiment commences, we will use the SSR measured on the day of the experiment by the *Total and Spectral Solar Irradiance Sensor* (TSIS) instrument on ISS and made available at [lasp.colorado.edu/tsis/data/](http://lasp.colorado.edu/tsis/data/) (see Harder et al., 2022) to model TSBR and SSBR.

Finally, in Section 5, we discuss and present our concluding remarks.

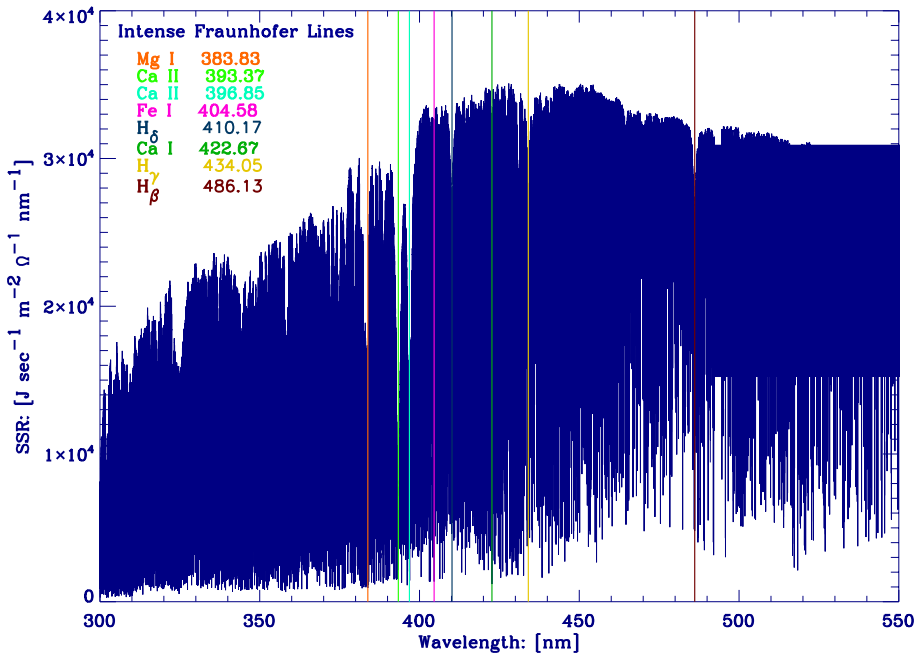


**Figure 1** Solar Spectral Radiance (SSR) in  $\text{J s}^{-1} \text{m}^{-2} \Omega^{-1} \text{nm}^{-1}$  as a function of wavelength in nm. Also shown are the locations of conspicuous, intense Fraunhofer lines. The wavelength resolution of the data is 0.00025 nm.

## 2. Measuring Polarized Brightness

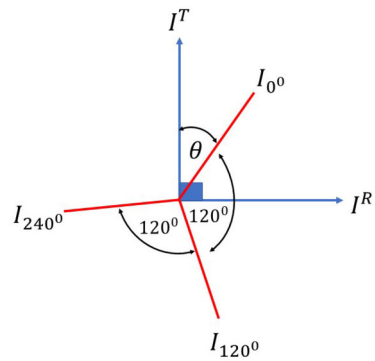
First, we present in Equation 1 the relationship between the experimentally measured pB and the three coronal images  $I_{0^\circ}$ ,  $I_{120^\circ}$ , and  $I_{240^\circ}$  taken consecutively through a linear polarizer by rotating the linear polarizer through three angles  $0^\circ$ ,  $120^\circ$ , and  $240^\circ$ , respectively. Equation 1 was derived by Billings (1966, p. 96) by considering the image brightness  $I_\theta$  related to the polarized brightness  $I_p$  and unpolarized brightness  $I_{up}$  by  $I_\theta = I_p \cos^2 \theta + \frac{I_{up}}{2}$ .

$$pB = \frac{4}{3} \sqrt{(I_{0^\circ} + I_{120^\circ} + I_{240^\circ})^2 - 3(I_{0^\circ} I_{120^\circ} + I_{0^\circ} I_{240^\circ} + I_{120^\circ} I_{240^\circ})}. \tag{1}$$

$$\begin{aligned}
 I_{0^\circ} &= I^T \cos^2(\theta) + I^R \cos^2(90^\circ - \theta) + \frac{I_{up}}{2}, \\
 I_{120^\circ} &= I^T \cos^2(120^\circ + \theta) + I^R \cos^2(30^\circ + \theta) + \frac{I_{up}}{2}, \\
 I_{240^\circ} &= I^T \cos^2(240^\circ + \theta) + I^R \cos^2(150^\circ + \theta) + \frac{I_{up}}{2}.
 \end{aligned} \tag{2}$$

However, in this article, we focus on finding the relationship between measured pB and modeled pB, which requires deriving the theoretical expression for  $I^T - I^R$  and show that the RHS of Equation 1 also measures  $I^T - I^R$ . So, in Figure 2, we show the orientations of  $I^T$  and  $I^R$ , which are mutually orthogonal, the three orientations of the linear polarizer  $I_{0^\circ}$ ,  $I_{120^\circ}$ , and  $I_{240^\circ}$ , which are  $120^\circ$  apart and shown in red, and the initial position  $I_{0^\circ}$  of

**Figure 2** Orientations of the tangential  $I^T$  and radial  $I^R$  components of the Thomson-scattered spectral radiance with respect to the three orientations of the linear polarizer  $I_{0^\circ}$ ,  $I_{120^\circ}$ , and  $I_{240^\circ}$ , which are  $120^\circ$  apart and are shown in red. The initial position of the linear polarizer is oriented at an arbitrary angle  $\theta$  with respect to  $I^T$ .  $I^T$  and  $I^R$  are mutually orthogonal to each other.



the linear polarizer being oriented at an arbitrary angle  $\theta$  with respect to  $I^T$ . Equation 2 shows the components of  $I^T$ ,  $I^R$ , and  $I_{up}$  along the directions of  $I_{0^\circ}$ ,  $I_{120^\circ}$ , and  $I_{240^\circ}$ . From Equation 2 we can obtain the right-hand side of Equation 1 for  $I^T - I^R$ .

Second, we present in Equation 3 the relationship between the experimentally measured pB and the four coronal images  $I_{0^\circ}$ ,  $I_{45^\circ}$ ,  $I_{90^\circ}$ , and  $I_{135^\circ}$  taken consecutively through a linear polarizer by rotating the linear polarizer through four angles  $0^\circ$ ,  $45^\circ$ ,  $90^\circ$ , and  $135^\circ$ , respectively, and derived by Billings (1966). The derivation of the expression for  $I^T - I^R$  from the four coronal images  $I_{0^\circ}$ ,  $I_{45^\circ}$ ,  $I_{90^\circ}$ , and  $I_{135^\circ}$  taken simultaneously using a polarization camera is presented in detail in Section 2 of Reginald, Newmark, and Rastaetter (2019), which matches the right-hand side of Equation 3.

$$pB = \sqrt{(I_{0^\circ} - I_{90^\circ})^2 + (I_{45^\circ} - I_{135^\circ})^2}. \tag{3}$$

### 3. Modeling Polarized Brightness Spectrum

In this section, we present the theoretically derived expressions for  $I^T$  and  $I^R$  to determine  $I^T - I^R$  for the three pB models  $pB_{N_e}$ ,  $pB_{N_e T_e}$ , and  $pB_{N_e T_e V_e}$ .

#### 3.1. Modeling Polarized Brightness as a Function of Electron Density

The earliest derivation of theoretical expressions for  $I^T$  and  $I^R$  can be traced back to Schuster (1879), who realized that accurately measuring the polarization of the light sent out by the solar corona will most likely give some important information on the nature of the Sun’s surroundings. Schuster sought a solution by calculating the polarization due to the scattering of light by a single particle placed close to a luminous sphere and then extending the calculation to include all the particles located along the line of sight, but not knowing the law that governs the distribution of particles around a luminous sphere. Schuster attempted to obtain a rough idea on the distribution of scattering particles in the solar corona using measured pB with coronal height during total solar eclipses. The limb-darkening effect was not considered. Expanding on Shuster’s work, Minnaert (1930) formulated the expressions for  $I^T$  and  $I^R$  that took into account the geometric factors determining the total integrated Thomson-scattered brightness along a line of sight, the effect of limb darkening on the Thomson-scattered brightness, and the Thomson-scattering cross-section. This work by Minnaert (1930) was followed by that of van de Hulst (1950), who showed how  $N_e$  can be derived by an inversion of the Abelian integral from measured pB during total solar eclipses

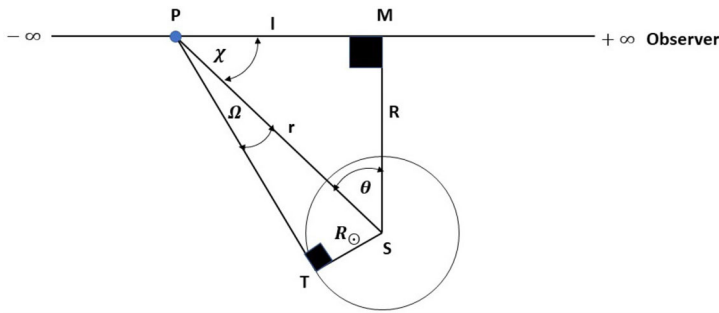


**Figure 3** A schematic showing the parameters used to compute the total integrated brightness of  $I^T$  and  $I^R$  along a line of sight that extends from the observer to  $\infty$ .

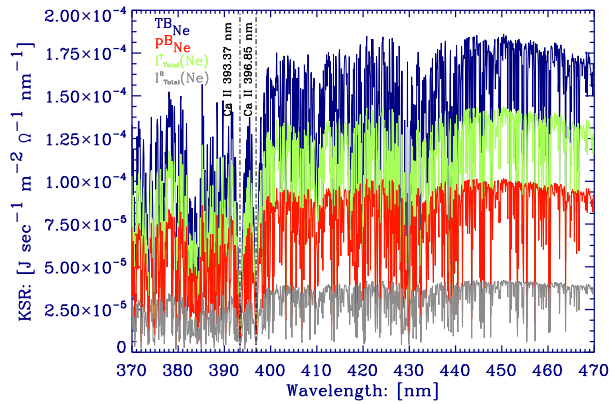
or using a coronagraph. Billings (1966, Chapter 6), summarizes all these previous works and provides a detailed derivation of the expressions for the brightness of  $I^T$  and  $I^R$  by a “single scattering condensation”. The formulation for the integrated brightness of  $I^T$  and  $I^R$  from all the scattering condensations along the line of sight was presented by Hundhausen (1993). In the present article, we only reproduce the two expressions along with the geometrical configuration we have used to compute the total integrated brightness of  $I^T$  and  $I^R$  given by  $I_{\text{Total}}^T(N_e)$  and  $I_{\text{Total}}^R(N_e)$ , respectively.

Figure A1 from Hundhausen (1993) shows a useful schematic for computing the Thomson-scattered radiance of SSR. In Figure 3 the plane of the drawing consists of the Sun center S and the line of sight through the corona where M is the point on the line of sight closest to the Sun center at a heliocentric distance R. Also shown are the angular displacement PSM of point P on the line of sight from the plane of sky defined by the plane perpendicular to the plane of the drawing and passing through the line SM, the angle between the radius through point P from Sun center and the line of sight SPM, and the angle between SP and a tangent from point P to the Sun’s surface TPS given by  $\theta$ ,  $\chi$ , and  $\Omega$ , respectively. For the electron density  $N_e(r/R_\odot)$ , where  $r$  is the distance from Sun center to any point in the solar corona, and  $R_\odot$  is the solar radius, we use Equation 14 in Baumbach (1937)

$$N_e\left(\frac{r}{R_\odot}\right) = \left(\frac{3.6 \times 10^6}{\left(\frac{r}{R_\odot}\right)^{1.5}} + \frac{1.55 \times 10^8}{\left(\frac{r}{R_\odot}\right)^6} + \frac{2.99 \times 10^8}{\left(\frac{r}{R_\odot}\right)^{16}}\right) \times 10^6 \left[\frac{1}{\text{m}^3}\right]. \quad (4)$$

Then the total integrated brightness of  $I^T$  is  $I_{\text{Total}}^T(N_e)$ , the total integrated brightness of  $I^R$  is  $I_{\text{Total}}^R(N_e)$ , the total polarized K-corona brightness is  $\text{pB}_{N_e}$ , and the total K-corona brightness is  $\text{TB}_{N_e}$ , and they are shown in Equation 5. Equation 5 matches the equations shown by Hundhausen (1993) on p. 13190 with modifications. The expressions for A, B, C, and D are shown in Hundhausen (1993) and are functions of the half angle  $\Omega$  subtended by the Sun when viewed from a heliocentric distance  $r$  where  $\sin(\Omega) = R_\odot/r$ . Also, the integrands in Equation 5 are the same as Equations 18 and 19 on p. 150 of Billings (1966), where from Figure 3  $\sin^2(\chi) = \cos^2(\theta)$ . We know that the limb-darkening coefficient  $u$  is wavelength dependent. Also, the empirical term  $(1 - u + u \cos \psi)$  used to account for limb-darkening shown in Equation 13 on p. 149 of Billings (1966) is replaced with  $(1 - u + u \cos \psi)/(1 - u/3)$  from Section 4 in van de Hulst (1950). In this article, we have changed the differential  $dl$  in Equation 5 in terms of the differential  $d\theta$  where  $dl = R d\theta / \cos^2 \theta$ ,  $r = R \cos \theta$ , and the limits of the integration go from  $-\pi/2$  to  $+\pi/2$ . [Note:

**Figure 4**  $I_{\text{Total}}^{\text{T}}(N_e)$ ,  $I_{\text{Total}}^{\text{R}}(N_e)$ ,  $\text{pB}_{N_e}$ , and  $\text{TB}_{N_e}$  from Equation 5, as measured by the observer shown in Figure 3, in the wavelength region from 370.0 nm to 470.0 nm and the line of sight passing at a distance  $R$  equal to  $3.0 R_{\odot}$  from Sun center. The wavelength resolution of the data is 0.1 nm.



Because of the  $\cos^2 \theta$  in the denominator of Equation 5, we have integrated from  $-89.9^\circ$  to  $+89.9^\circ$ .] This singularity arises when  $dl$  is expressed in terms of  $d\theta$ . For  $I_o$ , we used the SSR, for  $u_\lambda$ , we used Equation 18 in Cram (1976), and for  $\sigma$ , we used Equation 5 on p. 145 of Billings (1966), which is  $7.95 \times 10^{-30} \text{ m}^2 \Omega^{-1}$ . [Note: In Billings (1966) the  $\text{cm}^2$  term for units of  $\sigma$  is missing.] Then the units of K-corona spectral radiance (KSR) components  $I_{\text{Total}}^{\text{T}}(N_e)$  and  $I_{\text{Total}}^{\text{R}}(N_e)$  are in units of  $\text{J s}^{-1} \text{ m}^{-2} \Omega^{-1} \text{ nm}^{-1}$ . This is because the units of the parameters  $I_o$ ,  $\sigma$ ,  $(A, B, C, D)$ ,  $N_e$ , and  $dl$  in Equation 5 are  $\text{J s}^{-1} \text{ m}^{-2} \Omega^{-1} \text{ nm}^{-1}$ ,  $\text{m}^2 \Omega^{-1}$ ,  $\Omega$ ,  $\text{m}^{-3}$ , and  $\text{m}$ , respectively.

$$\begin{aligned}
 I_{\text{Total}}^{\text{T}}(N_e) &= \frac{\pi \sigma I_o}{2} \int_{-\infty}^{+\infty} N_e(r) \left[ \frac{1 - u_\lambda}{1 - \frac{u_\lambda}{3}} \times C + \frac{u_\lambda}{1 - \frac{u_\lambda}{3}} \times D \right] dl \\
 &\quad \left[ \frac{\text{J}}{\text{s m}^2 \Omega \text{ nm}} \right], \\
 I_{\text{Total}}^{\text{R}}(N_e) &= \frac{\pi \sigma I_o}{2} \int_{-\infty}^{+\infty} N_e(r) \left[ \frac{1 - u_\lambda}{1 - \frac{u_\lambda}{3}} \times (C - A \cos^2 \theta) \right. \\
 &\quad \left. + \frac{u_\lambda}{1 - \frac{u_\lambda}{3}} \times (D - B \cos^2 \theta) \right] dl \left[ \frac{\text{J}}{\text{s m}^2 \Omega \text{ nm}} \right], \\
 \text{pB}_{N_e} &= I_{\text{Total}}^{\text{T}}(N_e) - I_{\text{Total}}^{\text{R}}(N_e), \\
 \text{TB}_{N_e} &= I_{\text{Total}}^{\text{T}}(N_e) + I_{\text{Total}}^{\text{R}}(N_e). \tag{5}
 \end{aligned}$$

In Figure 4, we plot  $I_{\text{Total}}^{\text{T}}(N_e)$ ,  $I_{\text{Total}}^{\text{R}}(N_e)$ ,  $\text{pB}_{N_e}$ , and  $\text{TB}_{N_e}$  from Equation 5, as measured by the observer shown in Figure 3, in the wavelength region from 370.0 nm to 470.0 nm in intervals of 0.1 nm along the line of sight passing at a distance of  $R$  equal to  $3.0 R_{\odot}$  from Sun center in Figure 3. Also plotted are the two Fraunhofer lines Ca II K at 393.37 nm and Ca II H at 396.85 nm. The following are a list of some important observations from Figure 4.

- van de Hulst (1950) showed how  $\text{pB}_{N_e}$  measured through a broadband filter in visible light can be used to measure  $N_e$ . This required inverting the radial distribution of  $\text{pB}$  in the plane of sky by assuming it to follow a polynomial function. An example of implementing this inversion technique by van de Hulst (1950) to derive the  $N_e$  profile using  $\text{pB}$  images obtained from COR 1, COR 2, and LASCO-C2 instruments is presented by Morgan (2015) and Wang et al. (2017). Furthermore, in Fig-

ure 17b of Wang et al. (2017), they compared their results with the  $N_e$  profiles derived by Saito, Poland, and Munro (1977), Guhathakurta, Holzer, and MacQueen (1996), Leblanc, Dulk, and Bougeret (1998), and Gibson et al. (2006). In this comparison, Wang et al. (2017) found the results from Leblanc, Dulk, and Bougeret (1998) given by  $N_e(\frac{r}{R_\odot}) = (\frac{3.3 \times 10^5}{(\frac{r}{R_\odot})^2} + \frac{4.1 \times 10^6}{(\frac{r}{R_\odot})^4} + \frac{8.0 \times 10^7}{(\frac{r}{R_\odot})^6}) \times 10^6 [\frac{1}{\text{m}^3}]$  to best match their results for  $r$  between  $1.5 R_\odot$  and  $3.5 R_\odot$  from the Sun center, which we will call  $N_e^L$ . Baumbach (1937, 1938), using photometric measurements taken during ten total solar eclipses from 1905 to 1929 and assuming a spherically symmetric electron-density distribution, computed the first empirical expression for  $N_e$ , as shown in Equation 4, which produced the best match for  $r$  between  $1.05 R_\odot$  and  $3.0 R_\odot$  from Sun center, which we will call  $N_e^B$ . At that time the two components of pB,  $I^T$  and  $I^R$ , were not known, and the F-corona brightness attributed to the photospheric spectrum scattering off the interplanetary meteoritic dust and the K-corona brightness were not separated by polarization measurements, which would have obviously resulted in overestimation of  $N_e$ . Surprisingly,  $N_e^B$  produced the best match to the  $N_e$  profile computed by November and Koutchmy (1996) between  $1.0 R_\odot$  and  $1.7 R_\odot$  from Sun center during a unique opportunity, which allowed them to measure pB when the total solar eclipse of 11 July 1991 passed above the 3.6 m Canada–France–Hawaii (CHFT) telescope on Maunakea, Hawaii. In this article, we have used the  $N_e^B$  profile to represent  $N_e$ , which is  $\approx 10.0$  times denser than  $N_e^L$  and can also cause the coronal environment  $\approx 10.0$  times brighter.

- The KSR plots follow the shape of SSR shown in Figure 1, and the two deep and conspicuous Fraunhofer lines Ca II H and Ca II K from the SSR are clearly seen, which is troublesome. This is because the KSR plots are expected to be smooth from electrons with high  $T_e$  of several mega-Kelvins to thermal Doppler broaden the SSR and in the process to fill in the valleys and level the peaks in the millions of tiny absorption lines in the SSR. In the KSR plots, only residual depressions are expected to be seen in the locations of Fraunhofer lines, as first observed and reported by Grotrian (1931). However, producing a smoothed Thomson-scattered SSR using Equation 5 is not possible. This is because Equation 5 has no  $T_e$  dependency to thermal Doppler broaden the SSR and make it smooth. This results in the Thomson-scattered spectrum to match the features of the SSR spectrum with one-to-one correspondence but at a reduced magnitude.

### 3.2. Modeling Polarized Brightness as a Function of Electron Density and Temperature

A major deficiency in Figure 4 is that the KSR spectrum continues to follow the shape of the SSR. The expectation from observations is for the peaks in the SSR to be leveled and the valleys in the SSR to be filled to create a much smoother KSR compared to the SSR. The only exceptions are restricted to wavelength locations of deep and conspicuous Fraunhofer lines to only show minor depressions. In this regard, van Houten (1950) presented a theoretical computation of the KSR at the Fraunhofer line at 400.0 nm, which has an equivalent width of 1.0 nm. Here van Houten (1950) assumed the electrons to have a temperature of 1.0 MK and a Maxwellian distribution of thermal speeds, which allowed for the thermal Doppler broadening of the SSR spectrum at 400.0 nm upon SSR Thomson scattering off the coronal electrons. In conclusion, van Houten (1950) pointed out that the Fraunhofer lines should indicate depressions as deep as 7% in the KSR as compared to the SSR. Furthermore, it was deemed that these depressions measured by Grotrian (1931) during total solar eclipses can be used to measure  $T_e$ . Taking into account all these ideas, Cram (1976) presented a theoretical model that not only accounted for  $N_e$ , but also accounted for  $T_e$ , and we call this

model  $pB_{N_e T_e}$ . Then the total integrated brightness of  $I^T$  is  $I_{Total}^T(N_e, T_e)$ , the total integrated brightness of  $I^R$  is  $I_{Total}^R(N_e, T_e)$ , the total polarized K-corona brightness is  $pB_{N_e T_e}$ , the total K-corona brightness is  $TB_{N_e T_e}$ , and they are shown in Equation 6, which also corresponds to Equation 12 in Cram (1976) with the delta function  $\delta(\lambda - \lambda' + 2b\lambda' \frac{u_\perp}{c})$  corresponding to Equation 8 in Cram (1976) and shown in Equation 10 in Cram (1976). One of the properties of the coronal electrons in the model by Cram (1976) is that the coronal electrons, while vibrating due to  $T_e$ , still remained static in location and oblivious to expectations of flowing away from the Sun as solar wind. The expressions shown in Equation 6 reflect a 4D finite integration over the distance  $x$  along the line of sight, angles of altitude  $\omega$ , where no radiation is incident on point P when  $\omega > \omega^*$ , and azimuth  $\varphi$  of the line joining the source point S to the scattering point P, and the wavelength  $\lambda$  of the photospheric radiation incident on the electron. The term  $\Delta$  in Equation 6 is a function of  $T_e$ . The terms  $Q^R(\alpha, \Theta)$ ,  $Q^T(\alpha, \Theta)$ , and  $I_{\lambda'}(\omega, \varphi)$  are shown in Equation 7 and correspond to Equations 4, 5, and 17 in Cram (1976), respectively, and the expressions to transform  $(\alpha, \Theta)$  in terms of  $(\omega, \varphi)$  are given by Equations 14 and 15 in Cram (1976). In the first term in the right-hand side of Equation 7, the term  $\frac{1}{\pi} \left(\frac{1AU}{R_\odot}\right)^2$  is the reciprocal of the solid angle subtended by the Sun at 1.0 AU, and the term  $F_\lambda$  is the solar spectral irradiance, and they have units  $\Omega^{-1}$  and  $J s^{-1} m^{-2} nm^{-1}$ , respectively, and the product of these two terms is the SSR, which is plotted in Figure 1. The second term in the right-hand side of Equation 7 quantifies the surface brightness of the part of the Sun's surface when observed at an angle  $\theta$  to the normal due to the effect of limb-darkening, which is the exact form used in Section 3.1. Note that  $\sigma$  in Equation 7 is the Thomson scattering cross-section, and its value is  $6.677 \times 10^{-29} m^2$  as given by Equation 3 in Cram (1976) and by Equation 6 on p. 146 of Billings (1966). Then the units of KSR components  $I_{Total}^T(N_e, T_e)$  and  $I_{Total}^R(N_e, T_e)$  are  $J s^{-1} m^{-2} \Omega^{-1} nm^{-1}$ . This is because the units of the parameters  $I_{\lambda'}(\omega, \varphi)$ ,  $\sigma$ ,  $N_e$ ,  $\Delta^{-1}$ ,  $dx$ , and  $d\lambda'$  in Equation 6 are  $J s^{-1} m^{-2} \Omega^{-1} nm^{-1}$ ,  $m^2$ ,  $m^{-3}$ ,  $m^{-1}$ ,  $m$ , and  $m$ , respectively.

$$\begin{aligned}
 I_{Total}^T(N_e, T_e) &= \int_{-\infty}^{+\infty} dx N_e(x) \int_{\cos(\omega^*)}^1 d \cos(\omega) \int_0^{2\pi} d\varphi Q^T(\omega, \varphi) \\
 &\quad \times \int_0^\infty d\lambda' I_{\lambda'}(\omega, \varphi) \frac{e^{-((\lambda-\lambda')/2\Delta b)^2}}{2\sqrt{\pi} \Delta b} \left[ \frac{J}{s m^2 \Omega nm} \right], \\
 I_{Total}^R(N_e, T_e) &= \int_{-\infty}^{+\infty} dx N_e(x) \int_{\cos(\omega^*)}^1 d \cos(\omega) \int_0^{2\pi} d\varphi Q^R(\omega, \varphi) \\
 &\quad \times \int_0^\infty d\lambda' I_{\lambda'}(\omega, \varphi) \times \frac{e^{-((\lambda-\lambda')/2\Delta b)^2}}{2\sqrt{\pi} \Delta b} \left[ \frac{J}{s m^2 \Omega nm} \right], \\
 pB_{N_e T_e} &= I_{Total}^T(N_e, T_e) - I_{Total}^R(N_e, T_e), \\
 TB_{N_e T_e} &= I_{Total}^T(N_e, T_e) + I_{Total}^R(N_e, T_e). \tag{6}
 \end{aligned}$$

$$\begin{aligned}
 Q^R(\alpha, \Theta) &= \frac{3}{16} \sigma (\cos^2 \alpha \cos^2 \Theta + \sin^2 \alpha), \\
 Q^T(\alpha, \Theta) &= \frac{3}{16} \sigma (\cos^2 \alpha + \sin^2 \alpha \cos^2 \Theta), \\
 I_\lambda(\cos \theta) &= \frac{1}{\pi} \left(\frac{1AU}{R_\odot}\right)^2 F_\lambda \times \frac{1 - u_\lambda + u_\lambda \cos \theta}{1 - u_\lambda/3} \left[ \frac{J}{s m^2 \Omega nm} \right]; \tag{7}
 \end{aligned}$$

**Figure 5**  $I_{\text{Total}}^T(N_e, T_e)$ ,  $I_{\text{Total}}^R(N_e, T_e)$ ,  $pB_{N_e T_e}$ , and  $TB_{N_e T_e}$  from Equation 6 in the wavelength region from 370.0 nm to 470.0 nm with the line of sight passing at a distance  $\rho$  equal to  $3 R_{\odot}$  from Sun center and with  $T_e$  equal to 1.0 MK. The wavelength resolution of the data is 0.1 nm.

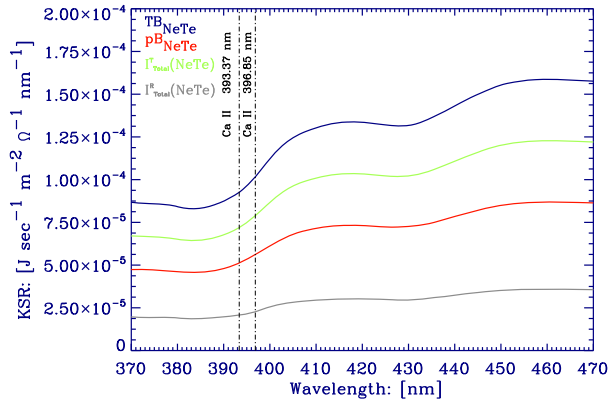
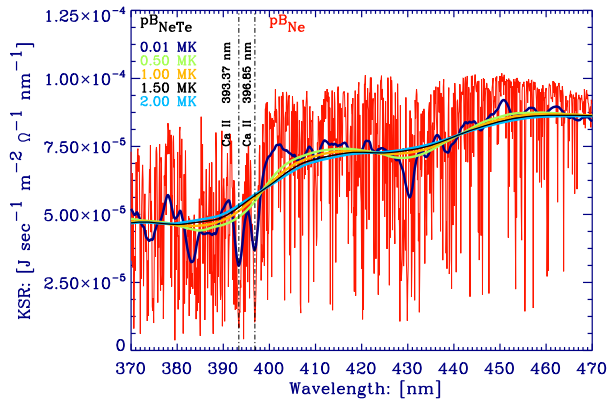


**Figure 6** Comparison of  $pB_{N_e}$  with  $pB_{N_e T_e}$  for  $T_e = 0.01, 0.5, 1.0, 1.5,$  and  $2.0$  MK. The wavelength resolution of the data is 0.1 nm.



where  $\omega^* = \sin^{-1}(1/r)$  and  $r$  is the distance between Sun center and P in  $R_{\odot}$ .

Figure 5 is a plot of Equation 6 showing  $I_{\text{Total}}^T(N_e, T_e)$ ,  $I_{\text{Total}}^R(N_e, T_e)$ ,  $pB_{N_e T_e}$ , and  $TB_{N_e T_e}$  for  $T_e$  equal to 1.0 MK,  $N_e$  given by Equation 4, and at a distance of  $\rho$  equal to  $3.0 R_{\odot}$  from Equation 13 in Cram (1976). Figure 5 is also the equivalent plot corresponding to Figure 4, where thermal Doppler broadening is taken into account. It is obvious that the profiles in Figure 5 are much smoother with the valleys and peaks in the SSR spectrum shown in Figure 1 being filled and flattened, respectively, upon Thomson scattering off the coronal electrons. Figure 6 compares  $pB_{N_e}$  with  $pB_{N_e T_e}$  for  $T_e = 0.01, 0.5, 1.0, 1.5,$  and  $2.0$  MK. From the shape of the  $pB_{N_e T_e}$  for  $T_e = 0.01$  MK we can infer that  $pB_{N_e T_e}$  begins to converge toward  $pB_{N_e}$  with lower and lower  $T_e$ . Cram (1976) names the temperature-sensitive wavelength locations as “anti-nodes” and temperature-insensitive wavelength locations as “nodes”. The following are a list of some important observations from Figures 5 and 6.

- The KSR plots follow the shape of SSR shown in Figure 1 but are much smoother. This observation satisfies the expectations of the KSR plots to be smooth, and it is evident that in the Thomson-scattering process the valleys and peaks in the SSR have been filled and flattened, respectively.
- The two deep and conspicuous Fraunhofer lines Ca II H and Ca II K from the SSR are clearly observed for  $T_e$  equal to 0.01 MK.

- Comparing the shape of the measured KSR using a spectrograph with shapes from modeled KSR for multitude of  $T_e$  values, we can measure  $T_e$  by finding the best matching model KSR with the measured KSR. The first to use this theoretical concept to measure  $T_e$  was by Ichimoto et al. (1996), who measured the KSR during the total solar eclipse of 3 November 1994 in Chile using a spectrograph. In conclusion, the shape of the measured KSR is a measure of  $T_e$ .

### 3.3. Modeling Polarized Brightness as a Function of Electron Density, Temperature, and Velocity

A major deficiency in Equation 6 is that the free coronal electrons are oblivious to the solar-wind flow, which takes a radial direction away from the Sun around  $2.5 R_\odot$  from Sun center. Here  $V_e$  accounts for the free coronal electrons streaming away from the Sun at a bulk flow velocity equal to the solar-wind velocity. Here we assume  $V_e$  to be directed outward from Sun center in a radial direction. Henceforth, we will simply call  $V_e$  the radial (rad) velocity  $V_{\text{rad}}$ . In reality, the coronal region between the solar limb to about  $2.5 R_\odot$  from Sun center the magnetic field and solar-wind flows are highly nonradial, and above this coronal region, the magnetic field and solar-wind flows become highly radial.

From a historical perspective, Woltjer (1926a, 1926b) investigated the effect on the Thomson-scattered spectrum when the photosphere spectrum is incident on the electrons while they are in motion and concluded that the influence of motion on the Thomson-scattered spectrum as ineffective. In the rest frame of the electron, Cram (1976) considered Thomson scattering to be coherent (or elastic) if red-shifts of  $\approx 0.00025$  nm related to Compton scattering are considered to be negligible. However, in the rest frame of the observer the wavelength of the photosphere spectrum incident on the electrons can be altered in Thomson scattering if the electron is in motion. As for any motion of the electron, the only motion considered by Cram (1976) was the thermal motion attributed to  $T_e$  of the electrons that took the shape of a Maxwellian distribution with a mean electron thermal velocity defined by  $\sqrt{2k_B T_e / m_e}$  where  $k_B$  and  $m_e$  are the Boltzmann constant ( $1.381 \times 10^{-23} \text{ m}^2 \text{ kg s}^{-2} \text{ K}^{-1}$ ) and the mass of the electron ( $9.109 \times 10^{-31} \text{ kg}$ ), respectively (see Equation 17 in Cram, 1976). For a typical value of  $T_e$  equal to 1.0 MK, the mean electron thermal velocity is  $5508 \text{ km s}^{-1}$ . Due to this high mean thermal electron velocity, Cram (1976) deemed that the effect on the KSR due to the bulk-flow (or solar-wind) velocity of the electrons is negligible. As a result, Cram's model remained a function of  $N_e$  and  $T_e$  only. However, Ichimoto et al. (1996), who used Cram's model to measure  $T_e$ , recognized that the KSR as a result of  $V_{\text{rad}}$  should cause the "nodes" in Figure 6 to red-shift, but the model for pB given in Equation 1 in Ichimoto et al. (1996), which corresponds to Equation 12 in Cram (1976), did not account for this red-shift because the electrons were considered to remain static or unaffected by the solar wind. Reginald (2001) introduced dynamics by allowing the free coronal electrons to flow away from the Sun center with a bulk flow velocity  $V_{\text{rad}}$  in the direction of  $OP$  or in the radial direction in Figure 1 in Cram (1976). Now to account for  $V_{\text{rad}}$ , consider Figure 2 in Cram (1976), which shows an orthogonal triad (or a Cartesian coordinate system) with unit vectors  $(n_1, n_2, n_3)$  along the three mutually orthogonal directions. Accordingly, the direction vectors of the incident radiation  $[n_{\text{in}}]$  on an electron at point P and the scattered radiation  $[n_{\text{out}}]$  off that same electron at point P, and the total velocity  $W = V_{\text{rad}} + U$  of the electron at point P comprising of the thermal velocity  $U$  and the bulk flow velocity  $V_{\text{rad}}$  in the directions of the unit vectors  $(n_1, n_2, n_3)$  are shown in Equation 8.

$$n_{\text{in}} = (-\cos \gamma, \sin \gamma, 0),$$

$$\mathbf{n}_{\text{out}} = (\cos \gamma, \sin \gamma, 0),$$

$$\mathbf{W} = (U_{n_1} + V_{\text{rad}, n_1}, U_{n_2} + V_{\text{rad}, n_2}, U_{n_3} + V_{\text{rad}, n_3}). \tag{8}$$

Let the wavelength of the radiation incident on the electron from the photosphere be  $\lambda_{\text{pho}}$ , let the wavelength of the scattered radiation off the electron be  $\lambda_{\text{sca}}$ , and let the wavelength of the radiation observed be  $\lambda_{\text{obs}}$ . Then using the relativistic expressions for Doppler effect in light between  $(\lambda_{\text{pho}}, \lambda_{\text{sca}})$  and  $(\lambda_{\text{sca}}, \lambda_{\text{obs}})$  along the direction vectors and the associated components of  $\mathbf{W}$  shown in Equation 8, we show the steps to reach the relationship between  $(\lambda_{\text{pho}}, \lambda_{\text{obs}})$  in Equation 9. The resolved values along the orthogonal triad  $(n_1, n_2, n_3)$  are  $V_{\text{rad}} = (V_{\text{rad}, n_1}, V_{\text{rad}, n_2}, V_{\text{rad}, n_3}) = |\mathbf{V}_{\text{rad}}|(-\cos \omega \cos \gamma, \cos \omega \sin \gamma, \sin \omega)$ .

$$\lambda_{\text{obs}} = \lambda_{\text{sca}} \frac{(1 - \frac{\mathbf{n}_{\text{out}} \cdot \mathbf{W}}{c})^{1/2}}{(1 + \frac{\mathbf{n}_{\text{out}} \cdot \mathbf{W}}{c})^{1/2}},$$

$$\lambda_{\text{sca}} = \lambda_{\text{pho}} \frac{(1 + \frac{\mathbf{n}_{\text{in}} \cdot \mathbf{W}}{c})^{1/2}}{(1 - \frac{\mathbf{n}_{\text{in}} \cdot \mathbf{W}}{c})^{1/2}},$$

$$\lambda_{\text{obs}} \approx \lambda_{\text{pho}} \frac{(1 + \frac{(\mathbf{n}_{\text{in}} - \mathbf{n}_{\text{out}}) \cdot \mathbf{W}}{c})^{1/2}}{(1 - \frac{(\mathbf{n}_{\text{in}} - \mathbf{n}_{\text{out}}) \cdot \mathbf{W}}{c})^{1/2}} \text{ (for } W \ll c),$$

$$\lambda_{\text{obs}} \approx \lambda_{\text{pho}} (1 + \frac{(\mathbf{n}_{\text{in}} - \mathbf{n}_{\text{out}}) \cdot \mathbf{W}}{c}) \text{ (Taylor expansion),}$$

$$(\mathbf{n}_{\text{in}} - \mathbf{n}_{\text{out}}) \cdot \frac{\mathbf{W}}{c} = -2 \cos \gamma \frac{(U_{n_1} + V_{\text{rad}, n_1})}{c},$$

$$\lambda_{\text{obs}} = \lambda_{\text{pho}} [1 - 2 \cos \gamma \frac{(U_{n_1} + V_{\text{rad}, n_1})}{c}]. \tag{9}$$

Then from Equation 9 the condition for coherent scattering in the rest frame of the electron is given by Equation 10, which is the new delta function, where  $b = \cos \gamma$ , and the first three terms match the delta function in Cram (1976). Here the red-shift due to Compton effect is considered negligible, which is true in the white-light wavelength region. However, in the rest frame of the observer,  $\lambda_{\text{pho}}$  will be altered due to the motion of the electron.

$$\lambda_{\text{obs}} - \lambda_{\text{pho}} + \frac{2 \cos \gamma U_{n_1}}{c} \lambda_{\text{pho}} + \frac{2 \cos \gamma V_{\text{rad}, n_1}}{c} \lambda_{\text{pho}} = 0,$$

$$\delta(\lambda_{\text{obs}} - \lambda_{\text{pho}} + 2b \lambda_{\text{pho}} \frac{U_{n_1}}{c} + 2b \lambda_{\text{pho}} \frac{V_{\text{rad}, n_1}}{c}). \tag{10}$$

To compute the net scattering of  $\lambda_{\text{pho}}$  off the electron density distribution at any given point P on the line of sight, we need to integrate over the velocity distribution at P. Here a Maxwellian velocity distribution is assumed. Then the number of electrons at P per unit volume and the velocity in the interval  $(\mathbf{U}, \mathbf{U} + d\mathbf{U})$  are given by Equation 11 (see Equation 6 in Cram, 1976), where  $q$  is the mean thermal electron velocity (see Equation 7 in Cram, 1976), which depends on the electron temperature.

$$f_e(\mathbf{U}) = N_e \frac{1}{(\sqrt{\pi}q)^3} e^{-\frac{U^2}{q^2}}. \tag{11}$$

Now for incorporating,  $V_{\text{rad}}$  requires a modification of the integrand  $I$  in the right-hand side of Equation 8 in Cram (1976), and the new expression is shown in Equation 12, which takes into account the revised expression for coherent scattering in the rest frame of the electrons shown in Equation 10.

$$\begin{aligned}
 I &= \int_{-\infty}^{+\infty} N_e \frac{1}{(\sqrt{\pi}q)^3} e^{-\frac{U_{n_1}^2 + U_{n_2}^2 + U_{n_3}^2}{q^2}} \\
 &\times \delta(\lambda_{\text{obs}} - \lambda_{\text{pho}} + 2b\lambda_{\text{pho}}\frac{U_{n_1}}{c} + 2b\lambda_{\text{pho}}\frac{V_{\text{rad},n_1}}{c}) \\
 &\times dU_{n_1}dU_{n_2}dU_{n_3}.
 \end{aligned}
 \tag{12}$$

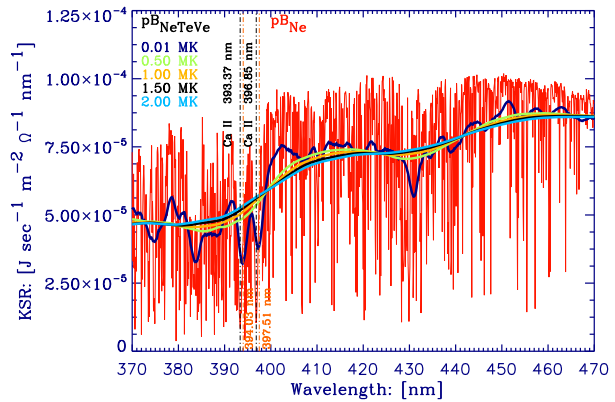
Writing  $|V_{\text{rad}}|$  as  $V_{\text{rad}}$  in the delta function in Equation 10, and using the relation  $\int_{-\infty}^{+\infty} e^{-ax^2} dx = \sqrt{\frac{\pi}{a}}$  and substituting  $\Delta = \frac{\lambda_{\text{pho}}}{c}q$  into Equation 12 gives Equation 13, which is the revised last two terms in the right-hand side of Equation 10 in Cram (1976). Now, using Equation 13 for the last two terms in the right-hand side of Equation 10 in Cram (1976) and with  $V_{\text{rad}} \neq 0 \text{ km s}^{-1}$ , we can reformulate Equation 12 in Cram (1976).

$$\begin{aligned}
 U_{n_1} &= -\frac{\lambda_{\text{obs}} - \lambda_{\text{pho}}(1 + 2b^2 \cos \omega \frac{V_{\text{rad}}}{c})}{\frac{2b\lambda_{\text{pho}}}{c}}, \\
 I &= N_e \frac{e^{-[\frac{\lambda_{\text{obs}} - \lambda_{\text{pho}}(1 + 2b^2 \cos \omega \frac{V_{\text{rad}}}{c})}{2\Delta b}]^2}}{2\sqrt{\pi} \Delta b}.
 \end{aligned}
 \tag{13}$$

Then the total integrated brightness of  $I^T$  is  $I^T_{\text{Total}}(N_e, T_e, V_e)$ , the total integrated brightness of  $I^R$  is  $I^R_{\text{Total}}(N_e, T_e, V_e)$ , the total polarized K-corona brightness is  $\text{pB}_{N_e T_e V_e}$ , and the total K-corona brightness is  $\text{TB}_{N_e T_e V_e}$ , and they are shown in Equation 14, with the notation used by Cram (1976) for  $\lambda_{\text{obs}}$  with  $\lambda$  and  $\lambda_{\text{pho}}$  with  $\lambda'$ . When  $V_{\text{rad}} = 0 \text{ km s}^{-1}$ , Equation 14 matches Equation 6. Figure 7 is a reproduction of Figure 6, where instead of Equation 6 for static coronal electrons, Equation 14 for dynamic coronal electrons is used with  $T_e = 0.01, 0.5, 1.0, 1.5,$  and  $2.0 \text{ MK}$  and  $V_{\text{rad}} = 500 \text{ km s}^{-1}$ . In Figure 7, it is obvious that the Ca II K line at  $393.37 \text{ nm}$  has red-shifted to  $394.03 \text{ nm}$ , and the Ca II H line at  $396.85 \text{ nm}$  has red-shifted to  $397.51 \text{ nm}$ . The whole KSR has red-shifted.

$$\begin{aligned}
 I^T_{\text{Total}}(N_e, T_e, V_e) &= \int_{-\infty}^{+\infty} dx N_e(x) \int_{\cos(\omega^*)}^1 d \cos(\omega) \int_0^{2\pi} d\varphi Q^T(\omega, \varphi) \\
 &\int_0^\infty d\lambda' I_{\lambda'}(\omega, \varphi) \frac{e^{-[\frac{\lambda - \lambda'(1 + 2b^2 \cos \omega \frac{V_{\text{rad}}}{c})}{2\Delta b}]^2}}{2\sqrt{\pi} \Delta b} \\
 &\left[ \frac{\text{J}}{\text{s m}^2 \Omega \text{ nm}} \right], \\
 I^R_{\text{Total}}(N_e, T_e, V_e) &= \int_{-\infty}^{+\infty} dx N_e(x) \int_{\cos(\omega^*)}^1 d \cos(\omega) \int_0^{2\pi} d\varphi Q^R(\omega, \varphi) \\
 &\int_0^\infty d\lambda' I_{\lambda'}(\omega, \varphi) \times \frac{e^{-[\frac{\lambda - \lambda'(1 + 2b^2 \cos \omega \frac{V_{\text{rad}}}{c})}{2\Delta b}]^2}}{2\sqrt{\pi} \Delta b} \\
 &\left[ \frac{\text{J}}{\text{s m}^2 \Omega \text{ nm}} \right],
 \end{aligned}$$

**Figure 7** Comparison of  $pB_{Ne}$  with  $pB_{NeT_eV_e}$  for  $T_e = 0.01, 0.5, 1.0, 1.5,$  and  $2.0$  MK and  $V_{rad} = 500 \text{ km s}^{-1}$ . The Ca II K line at  $393.37 \text{ nm}$  has red-shifted to  $394.03 \text{ nm}$ , and the Ca II H line at  $396.85 \text{ nm}$  has red-shifted to  $397.51 \text{ nm}$ . The wavelength resolution of the data is  $0.1 \text{ nm}$ .



$$\begin{aligned}
 pB_{NeT_eV_e} &= I_{Total}^T(N_e, T_e, V_e) - I_{Total}^R(N_e, T_e, V_e), \\
 TB_{NeT_eV_e} &= I_{Total}^T(N_e, T_e, V_e) + I_{Total}^R(N_e, T_e, V_e).
 \end{aligned}
 \tag{14}$$

The theoretically predicted red-shifting of the KSR due to  $V_{rad}$  by Reginald and Davila (2000) was independently experimentally investigated during the total solar eclipse of 26 March 2006 in Libya by Kim et al. (2017) and was confirmed “The reddening with distance is revealed for the whole corona indicating the red-shifting of the K-corona spectrum due to the outward bulk flow speed of the coronal electrons theoretically predicted by Reginald and Davila (2000) and Reginald et al. (2009).” The following is a list of some important observations from Figure 7.

- KSR follows the shape of SSR shown in Figure 1 but is much smoother and also red-shifted with radial flow speed  $V_{rad}$ . This is because the electrons see a red-shifted photospheric spectrum and this wavelength information is preserved in Thomson scattering.
- The two deep and conspicuous Fraunhofer lines Ca II H and Ca II K from the SSR are clearly observed for  $T_e$  equal to 0.01 MK to have red-shifted.
- By taking measurements of the KSR using a spectrograph and then comparing with KSR models both  $T_e$  and  $V_{rad}$  can be measured simultaneously, which means that the shape of the KSR is a measure of  $T_e$  and the red-shift of the KSR is a measure of  $V_{rad}$ . We call this the Spectrum Matching Technique (SMT). The first to use SMT to measure both  $T_e$  and  $V_{rad}$  simultaneously was Reginald (2001), who measured the KSR during the total solar eclipse of 11 August 1999 in Turkey using a spectrograph. Subsequent SMT measurements were taken during the total solar eclipses of 21 June 2001 in Zambia (see Reginald et al., 2003) and 29 March 2006 in Libya (see Reginald et al., 2011). The solar-wind plasma is highly conducting, and the magnetic field is frozen into the plasma. As a result, the magnetic field takes a spiral-like structure due to the rotation of the Sun and the outflow of the solar wind. Close to the Sun’s limb the magnetic-field forces dominate the plasma flow, and the direction of the flow cannot be deemed to be purely radial. As to where the flow becomes radial, the widely used Potential Field Source Surface (PFSS) model originally developed by Schatten, Wilcox, and Ness (1969) and Altschuler and Newkirk (1969) and refined by Hoeksema (1984) to derive the magnetic field of the corona assumes the source surface to originate at  $2.5 R_{\odot}$  from Sun center. Accordingly, at the source surface the pressure-driven expansion of the solar-wind becomes dominant and causes both the field and flow to be purely radial. In the heliosphere, the rotation of

the interplanetary magnetic field (IMF) foot points within the solar-wind flow generates an azimuthal component to the IMF, which leads to the spiral geometry.

- $V_{\text{rad}}$  can be measured in Thomson scattering even when the electrons are flowing away from the Sun perpendicular to the line of sight (or in the plane of sky).
- In Figures 9 and 10 in Reginald, Davila, and St. Cyr (2004), we considered five published  $N_e$  profiles found in the literature that were symmetric about the plane of sky for any given line of sight passing through the corona to study their effects on the shape of the modeled  $\text{pB}_{N_e T_e V_e}$  spectrum, in which, when normalized at 400.0 nm, we did not find any discernible differences. This is because in all these five  $N_e$  models, they rapidly drop off with  $r$ , and, as a result, for any given line of sight, only the electrons close to the plane of sky contribute most to the integrated pB along the line of sight. This scenario changes when coronal structures such as streamers and CMEs cross the line of sight away from the plane of sky in front or behind the plane of sky. In such situations the electron density at the crossing locations can become comparable to the electron density at the plane of sky and contribute to the integrated pB along that line of sight in a meaningful way. This condition will also make  $N_e$  asymmetric about the plane of sky for the lines of sight impacted by the coronal structure and will cause discernible differences in the shapes of the modeled  $\text{pB}_{N_e T_e V_e}$  spectra when compared with  $N_e$  profiles symmetric about the plane of sky. Asymmetric  $N_e$  profiles will also impact modeled TSBR and SSBR in FRT, and the associated systematic error in the measurements of  $T_e$  and  $V_e$  were discussed by Reginald et al. (2018), and how this systematic error can be corrected was discussed by Reginald, Newmark, and Rastaetter (2020). Cram (1976) also considered the impact of asymmetric  $N_e$  profiles on the shape of the modeled  $\text{pB}_{N_e T_e}$  spectrum.

From Figures 6 and 7 we see that the profiles of  $\text{pB}_{N_e}$ ,  $\text{pB}_{N_e T_e}$ , and  $\text{pB}_{N_e T_e V_e}$  have different shapes within the chosen wavelength range from 370.0 nm to 470.0 nm considered in this article. It is worth noting the importance of the influence of  $V_e$  in modeling pB although it may seem insignificant. This is because without accounting for  $V_e$  in modeling pB, we would not know how to select the temperature-sensitive filters for FRT experiments to model TSBR to be dependent on  $T_e$  but independent of  $V_e$  for the purpose of interpreting measured TSBR in terms of  $T_e$ , which is discussed in detail in Appendix C of Reginald et al. (2018). In the case of SMT experiments, using a measured pB spectrum to measure only  $T_e$ , which could have red-shifted with  $V_e$ , by matching with the shapes of modeled  $\text{pB}_{N_e T_e}$  spectra by Cram (1976) for different  $T_e$ , which are not subject to red-shifts, can lead to selecting the wrong modeled  $\text{pB}_{N_e T_e}$  spectrum as the best-fitting modeled pB spectrum to match the measured pB spectrum. This is tantamount to trying to match  $\text{pB}_{N_e T_e V_e}$  with modeled  $\text{pB}_{N_e T_e}$  spectra, which is possible only when  $V_e$  is zero. To reiterate,  $N_e$  determines the brightness of the pB spectrum,  $T_e$  determines the shape of the pB spectrum, and  $V_e$  determines the red-shift of the pB spectrum. Surely, the thermal velocity is much higher than the flow velocity, but their influences on the pB spectrum are fundamentally different. The flow velocity in the radial direction away from the Sun causes the electrons to see a red-shifted photospheric spectrum and the thermal-velocity Doppler broadens this already red-shifted photospheric spectrum. The wavelength information pertaining to the flow velocity is preserved in Thomson scattering because this process is elastic.

Next, we quantify the differences in the total integrated brightness between ( $\text{pB}_{N_e}$  and  $\text{pB}_{N_e T_e}$ ) and ( $\text{pB}_{N_e}$  and  $\text{pB}_{N_e T_e V_e}$ ) in three wavelength bands, broadband from  $420.0 \text{ nm} \pm 50.0 \text{ nm}$  that encompasses the entire wavelength range in both Figures 6 and 7, narrow band Ca II K from  $393.37 \pm 0.1 \text{ nm}$ , and narrow band Ca II H from  $396.85 \pm 0.1 \text{ nm}$ , and tabulate the results in Table 1 together with the percentage differences. From Table 1 we see that the results for  $\text{pB}_{N_e}$ ,  $\text{pB}_{N_e T_e}$ , and  $\text{pB}_{N_e T_e V_e}$  measured using the broadband filter are the same (see

**Table 1**  $pB_{N_e}$ ,  $pB_{N_e T_e}$ , and  $pB_{N_e T_e V_e}$  measured along a line of sight intersecting the plane of sky at  $3.0 R_{\odot}$  from Sun center for three cases using a broadband, Ca II K, and Ca II H filters and centered at 420.0 nm, 393.37 nm, and 396.85 nm, respectively, and with bandwidths of  $\pm 50.0$  nm,  $\pm 0.1$  nm, and  $\pm 0.1$  nm, respectively. Columns 5 and 6 show within parentheses the percentage difference of  $(X - pB_{N_e})/pB_{N_e} \times 100\%$  from row 1, where  $X$  are the  $pB_{N_e T_e}$  and  $pB_{N_e T_e V_e}$  values. NA = Not Applicable.

Model	$T_e$	$V_{\text{rad}}$	Broadband	Ca II K	Ca II H
			420.0 $\pm$ 50.0 nm	393.37 $\pm$ 0.1 nm	396.85 $\pm$ 0.1 nm
	MK	km s <sup>-1</sup>	J s <sup>-1</sup> m <sup>-2</sup> $\Omega^{-1} \times 10^{-3}$	J s <sup>-1</sup> m <sup>-2</sup> $\Omega^{-1} \times 10^{-4}$ [%]	J s <sup>-1</sup> m <sup>-2</sup> $\Omega^{-1} \times 10^{-4}$ [%]
$pB_{N_e}$	NA	NA	6.852	0.601, (NA)	0.810, (NA)
$pB_{N_e T_e}$	0.01	NA	6.898	0.716, (19.1)	0.841, (3.9)
	0.50	NA	6.901	0.982, (63.4)	1.099, (35.8)
	1.00	NA	6.897	1.025, (70.6)	1.125, (38.9)
	1.50	NA	6.892	1.053, (75.2)	1.138, (40.6)
	2.00	NA	6.887	1.069, (77.9)	1.146, (41.5)
$pB_{N_e T_e V_e}$	0.01	500	6.865	0.776, (29.1)	0.855, (5.5)
	0.50	500	6.864	0.965, (60.6)	1.074, (32.6)
	1.00	500	6.859	1.008, (67.7)	1.106, (36.6)
	1.50	500	6.854	1.036, (72.3)	1.122, (38.6)
	2.00	500	6.849	1.054, (75.3)	1.132, (39.8)

column 4), but the results are not the same for measurements using the Ca II K filter (see column 5) and Ca II H filter (see column 6). Within the parentheses in columns 5 and 6, there are the percentage differences between  $pB_{N_e}$  and  $pB_{N_e T_e}$  and between  $pB_{N_e}$  and  $pB_{N_e T_e V_e}$ . The percentage difference is calculated by the expression  $(X - pB_{N_e})/pB_{N_e} \times 100\%$ , where  $X$  is  $pB_{N_e T_e}$  and  $pB_{N_e T_e V_e}$ . We see from Table 1 that the differences can range from underestimating  $pB_{N_e}$  in comparison with  $pB_{N_e T_e}$  up to  $\approx 78\%$  through the Ca II K (393.37 nm) filter and up to  $\approx 42\%$  through the Ca II H (396.85 nm) filter.  $pB_{N_e}$  in comparison with  $pB_{N_e T_e V_e}$  can be underestimated up to  $\approx 75\%$  through the Ca II K filter and up to  $\approx 40\%$  through the Ca II H filter. Each of these two filters is assumed to have a bandwidth of  $\pm 0.1$  nm about their centers, and  $pB_{N_e}$ ,  $pB_{N_e T_e}$ , and  $pB_{N_e T_e V_e}$  were modeled in intervals of 0.1 nm within these bandwidths. These differences show a clear implication when attempting to subtract background K-corona brightness using  $pB_{N_e}$ , which depends only on  $N_e$  and is susceptible to underestimation. These differences are expected because with increasing  $T_e$  the valleys will be increasingly filled and the hills increasingly leveled in the SSR. So, over a broad band, the net effect will most likely sum up to zero, as seen in column 4. However, if we consider a narrow band centered on a Fraunhofer line, which is a valley, and with increasing  $T_e$ , then this valley will get increasingly filled only for  $pB_{N_e T_e}$  and  $pB_{N_e T_e V_e}$ , resulting in underestimation for  $pB_{N_e}$ , and with  $V_e$  this valley will get red-shifted only for  $pB_{N_e T_e V_e}$ , causing only a small difference between  $pB_{N_e T_e}$  and  $pB_{N_e T_e V_e}$ .

Next, we compare the degree of linear polarization (DOLP), which is defined by  $(I^T - I^R)/(I^T + I^R)$  and computed at wavelength equal to 433.0 nm,  $N_e$  equal to  $N_e^B$ ,  $T_e$  equal to 1.0 MK, and  $V_{\text{rad}}$  equal to 0.0 km s<sup>-1</sup> for various values of  $r$  in Table 3 in Shklovskii (1965), with the DOLP computed at the same wavelength by  $pB_{N_e}$  using  $N_e^B$ ,  $pB_{N_e T_e}$  using  $N_e^B$  and 1.0 MK, and  $pB_{N_e T_e V_e}$  using  $N_e^B$ , 1.0 MK, and 500.0 km s<sup>-1</sup>, and the results are tabulated in Table 2. We see in Table 2 that DOLP measured by  $pB_{N_e T_e}$  in column 4 and  $pB_{N_e T_e V_e}$  in column 5 closely match the results from Shklovskii (1965) in column 2.

**Table 2** Comparison of DOLP computed in Table 3 in Shklovskii (1965) at 433.0 nm with DOLP computed using the models  $pB_{N_e}$ ,  $pB_{N_e T_e}$ , and  $pB_{N_e T_e V_e}$ .

$r$ [ $R_\odot$ ]	Shklovskii Table 3	$pB_{N_e}$ $N_e^B$	$pB_{N_e T_e}$ $N_e^B$ , 1.0 MK	$pB_{N_e T_e V_e}$ $N_e^B$ , 1.0 MK, 500 km s <sup>-1</sup>
1.0	0.199	0.193	0.191	0.191
1.1	0.333	0.278	0.330	0.330
1.2	0.404	0.329	0.405	0.405
1.3	0.454	0.365	0.455	0.456
1.4	0.491	0.393	0.491	0.492
1.5	0.514	0.415	0.517	0.518
1.7	0.547	0.447	0.548	0.548
2.0	0.548	0.478	0.562	0.562
3.0	0.549	0.521	0.549	0.549
infinity	0.556	0.557	0.557	0.557

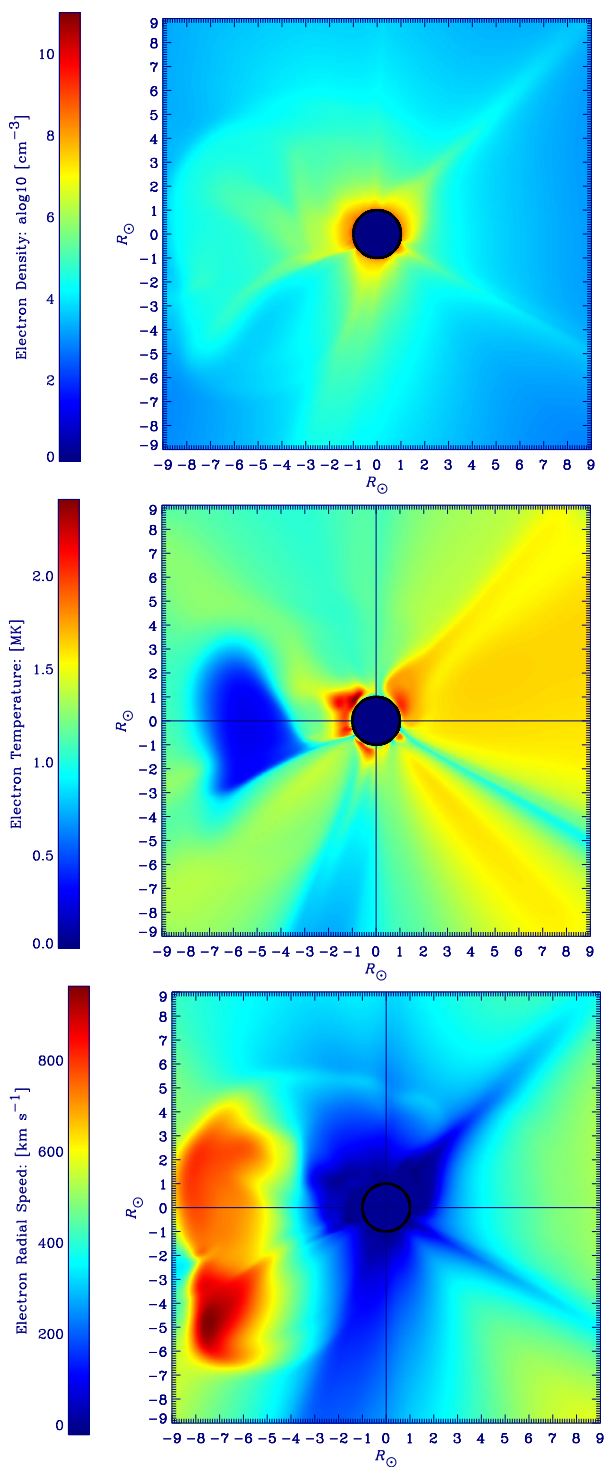
Reginald and Rastaetter (2019) present additional comparisons of DOLP measured using  $pB_{N_e T_e V_e}$  with DOLP computed by Shklovskii (1965) at 570.0 nm using the  $N_e^B$  model by Baumbach (1937), and the equatorial and polar  $N_e$  models by Saito et al. (1977). The results shown in Figure 5 in Reginald and Rastaetter (2019) show that DOLP computed using  $pB_{N_e T_e}$  and  $pB_{N_e T_e V_e}$  match very closely with Shklovskii (1965).

#### 4. Modeling Polarized Brightness Maps

In this section, we do simulations to produce 2D maps of  $pB_{N_e}$ ,  $pB_{N_e T_e}$ , and  $pB_{N_e T_e V_e}$ . These 2D maps are centered at Ca II H (396.85 nm) and Ca II K (393.37 nm) lines with a bandwidth of  $\pm 0.1$  nm about their centers. For this simulation, we use a realistic 3D model of the solar corona modeled by Török et al. (2018) to represent the Bastille Day CME. For each time step of this Bastille Day CME model, coronal model data are provided in the form of a data sphere that extends from 1.0  $R_\odot$  to 20.0  $R_\odot$  with respect to Sun center. For this analysis, we picked the model data sphere time stamped for 11:17:28 UT on 14 July 2000. This Bastille Day model data sphere by Török et al. (2018) contains, among other physical parameters, information on electron density, ion (proton) temperature, and ion (proton) speed. For our analysis, we have to assume that the ion temperature and speed match the electron temperature and speed. In Figure 8, we show the electron density ( $N_e$ , top), the electron temperature ( $T_e$ , middle), and the electron radial speed ( $V_{rad}$ , bottom) in the plane of sky, which extends to  $\pm 9.0 R_\odot$  from Sun center along the horizontal axis that lies on the Ecliptic plane and along the vertical axis perpendicular to the Ecliptic plane. Figure 8 has a image resolution of  $0.01 R_\odot \times 0.01 R_\odot$ .

To produce the 2D maps of  $pB_{N_e}$ ,  $pB_{N_e T_e}$ , and  $pB_{N_e T_e V_e}$ , we have to first decide on the coordinate system. For this, we use a Cartesian coordinate system ( $x$ ,  $y$ ,  $z$ ) with Sun center as its origin. The  $x$ -axis connects Sun center with Earth center, the  $y$ -axis is on the Ecliptic plane, and the  $z$ -axis is perpendicular to the Ecliptic plane. Then the  $yz$ -plane is the plane of sky. The square image plane for the 2D map in the plane of the sky is centered on the Sun center with the square grid extending from  $\pm 9.0 R_\odot$  along both the  $y$ -axis and  $z$ -axis. This square grid is then separated into 5329 ( $73 \times 73$ ) individual cells of size  $0.25 R_\odot \times 0.25 R_\odot$ , and 5329 lines-of-sight originating from the observer are then drawn through the centers of

**Figure 8** Electron density ( $N_e$ , *top*), electron temperature ( $T_e$ , *middle*), and the electron radial speed ( $V_{\text{rad}}$ , *bottom*) in the plane of sky extracted from the Bastille Day CME model (11:17:28 UT on 14 July 2000) used to compute 2D maps of  $\text{pB}_{N_e}$ ,  $\text{pB}_{N_e T_e}$ , and  $\text{pB}_{N_e T_e V_e}$ . Note:  $\text{alog}_{10}(x) = \log_{10}(x)$ .



these cells. Then the observer computes the  $pB$  corresponding to  $pB_{N_e}$ ,  $pB_{N_e T_e}$ , and  $pB_{N_e T_e V_e}$  for each line of sight that does not intersect with the solar disk using the following three-step process.

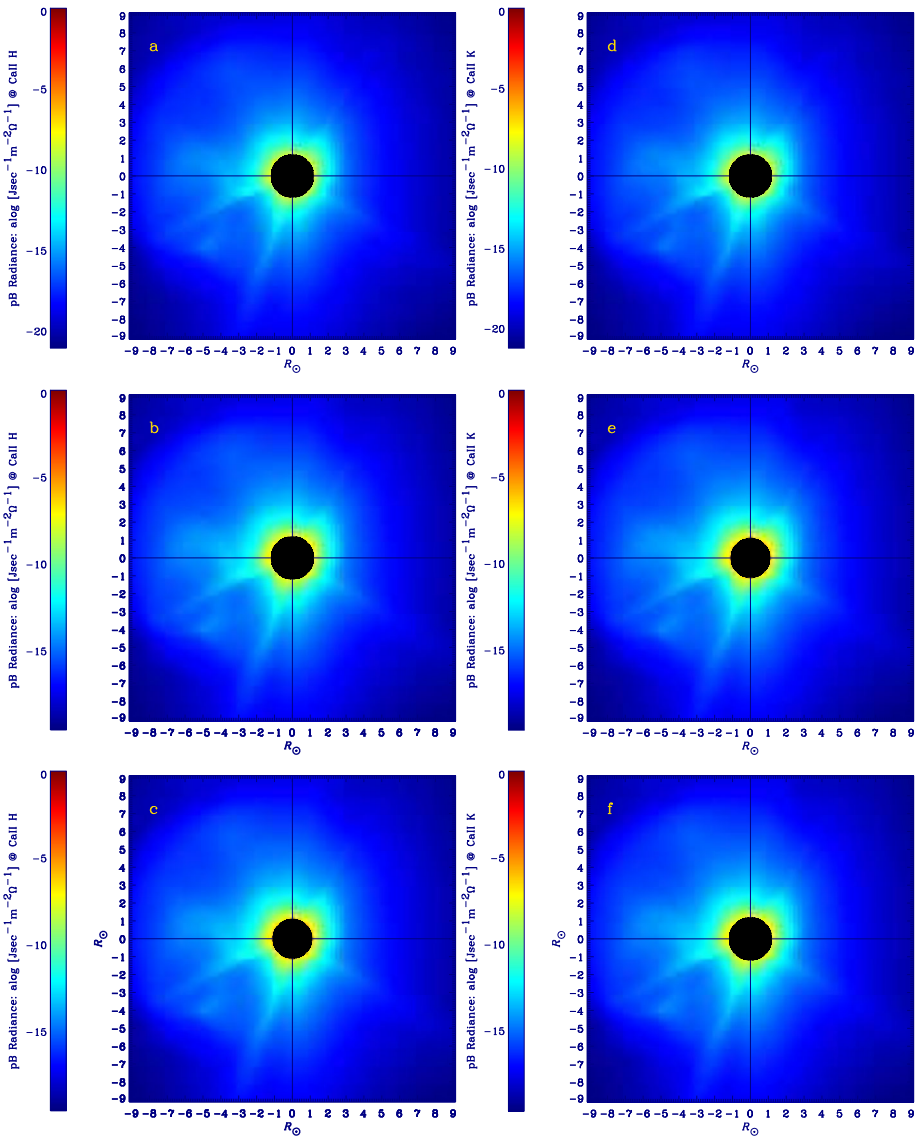
First, we have to find the two points of intersection of the selected line of sight with the Bastille Day CME model sphere (herein data sphere), which will be the entry point into the data sphere and the exit point out of the data sphere. Second, the length between the entry and exit points within the data sphere are divided into intervals of  $0.05 R_\odot$ , and at each of these intervals, which we call data points, we determine the Cartesian coordinates  $(x_i, y_i, z_i)$ , and the  $N_e$ ,  $T_e$ , and  $V_{\text{rad}}$  values at these data points are extracted from the data sphere using a simple trilinear interpolation. Third,  $pB_{N_e}$ ,  $pB_{N_e T_e}$ , and  $pB_{N_e T_e V_e}$  are computed using Equations 5, 6, and 14, respectively, with the solar spectrum shown in Figure 1 acting as the source for Thomson scattering. To elaborate, to compute  $pB_{N_e}$ , we use the likes of Figure 8 (top) at  $(x_i, y_i, z_i)$  in Equation 5. To compute  $pB_{N_e T_e}$ , we use the likes of Figure 8 (top, middle) at  $(x_i, y_i, z_i)$  in Equation 6. To compute  $pB_{N_e T_e V_e}$ , we use the likes of Figure 8 (top, middle, bottom) at  $(x_i, y_i, z_i)$  in Equation 14.

Figure 9 shows the integrated  $pB_{N_e}$  (top row),  $pB_{N_e T_e}$  (middle row), and  $pB_{N_e T_e V_e}$  (bottom row) in the wavelength regions of Ca II K (left column) using three images computed at wavelengths 393.27 nm, 393.37 nm, and 393.47 nm and of Ca II H (right column) using three images computed at wavelengths 396.75 nm, 396.85 nm, and 396.95 nm. Here the image resolution of  $0.25 R_\odot \times 0.25 R_\odot$  is very much lower than the image resolution of  $0.01 R_\odot \times 0.01 R_\odot$  in Figure 8. This is because it becomes computationally demanding in terms of processing time using a desktop computer to compute  $pB_{N_e T_e}$  and  $pB_{N_e T_e V_e}$ , whereas it only requires reading the data from the data sphere in the plane of sky to produce Figure 8. Visually, all six frames in Figure 9 look the same.

To quantify the differences in Figure 9, we present in Figure 10 the percentage differences between the six frames in Figure 9. For this computation, we use the symbols D for density, DT for density and temperature, and DTS for density, temperature, and speed to represent  $pB_{N_e}$ ,  $pB_{N_e T_e}$ , and  $pB_{N_e T_e V_e}$ , respectively. In Figure 10, we compute the percentage differences for Ca II H given by  $\frac{DT-D}{D} \times 100\%$  in Panel a,  $\frac{DTS-D}{D} \times 100\%$  in Panel b, and  $\frac{DT-DTS}{DTS} \times 100\%$  in Panel c, and the corresponding percentage differences for Ca II K in Figure 10 d, e, and f, respectively. Now, from Figure 10 a, b, d, and e we see that the percentage differences are high as 400% when DT and DTS are compared against D, and in Figure 10 c, and f when DTS is compared against DT the differences are high as 12%. Here again Ca II K and H are deep valleys in the SSR, and only in DT and DTS these valleys are filled due to  $T_e$ ; as a result, D is underestimated when compared with DT and DTS, whereas only DTS is subject to red-shifting due to  $V_{\text{rad}}$ .

In Figure 11, we show 2D maps of  $pB_{N_e}$  in Panel a,  $pB_{N_e T_e}$  in Panel b, and  $pB_{N_e T_e V_e}$  in Panel c at wavelength 530.3 nm integrated over a bandwidth of  $\pm 0.3$  nm about the center wavelength, in intervals of 0.1 nm, and spans from 530.0 nm to 530.6 nm. Here again Figure 11 a, b, and c look identical in features and magnitudes. To highlight any differences in magnitudes in Figure 11 a, b, and c, we show in Figure 11 d, e, and f the percentage differences  $\frac{DT-D}{D} \times 100\%$  in Panel d,  $\frac{DTS-D}{D} \times 100\%$  in Panel e, and  $\frac{DT-DTS}{DTS} \times 100\%$  in Panel f. From Figure 11 d and e we see a maximum difference of  $\approx -5\%$  due to the small hill in the SSR at  $530.3 \pm 0.3$  nm that gets flattened only for DT and DTS, and in Figure 11 f, we see only a maximum difference of  $\approx 1\%$ , where only DTS gets both flattened and red-shifted.

In Figure 12 a, b, and c, we show 2D DOLP maps, and in Figure 12 d, e, and f, we show the percentage differences. Here again the differences are minimal because the SSR in the wavelength region  $530.3 \pm 0.3$  nm is nearly flat. We also see in Figure 12 a, b, and



**Figure 9** Two-dimensional maps of  $pB_{N_c}$  (a, d),  $pB_{N_c T_c}$  (b, e), and  $pB_{N_c T_c V_c}$  (c, f), where the *left column* pertains to Ca II K at  $393.37 \text{ nm} \pm 0.1 \text{ nm}$ , and the *right column* pertains to Ca II K at  $396.85 \pm 0.1 \text{ nm}$ . Note:  $\log(x) = \log_c(x)$ .

c how DOLP can make coronal structures conspicuous, which then can be traced with time to estimate expansion and propagation times. This same coronal feature around 1900 UT in Figure 12 a, b, and c was traced with time in eight time intervals in Figure 6 by Reginald and Rastaetter (2019).

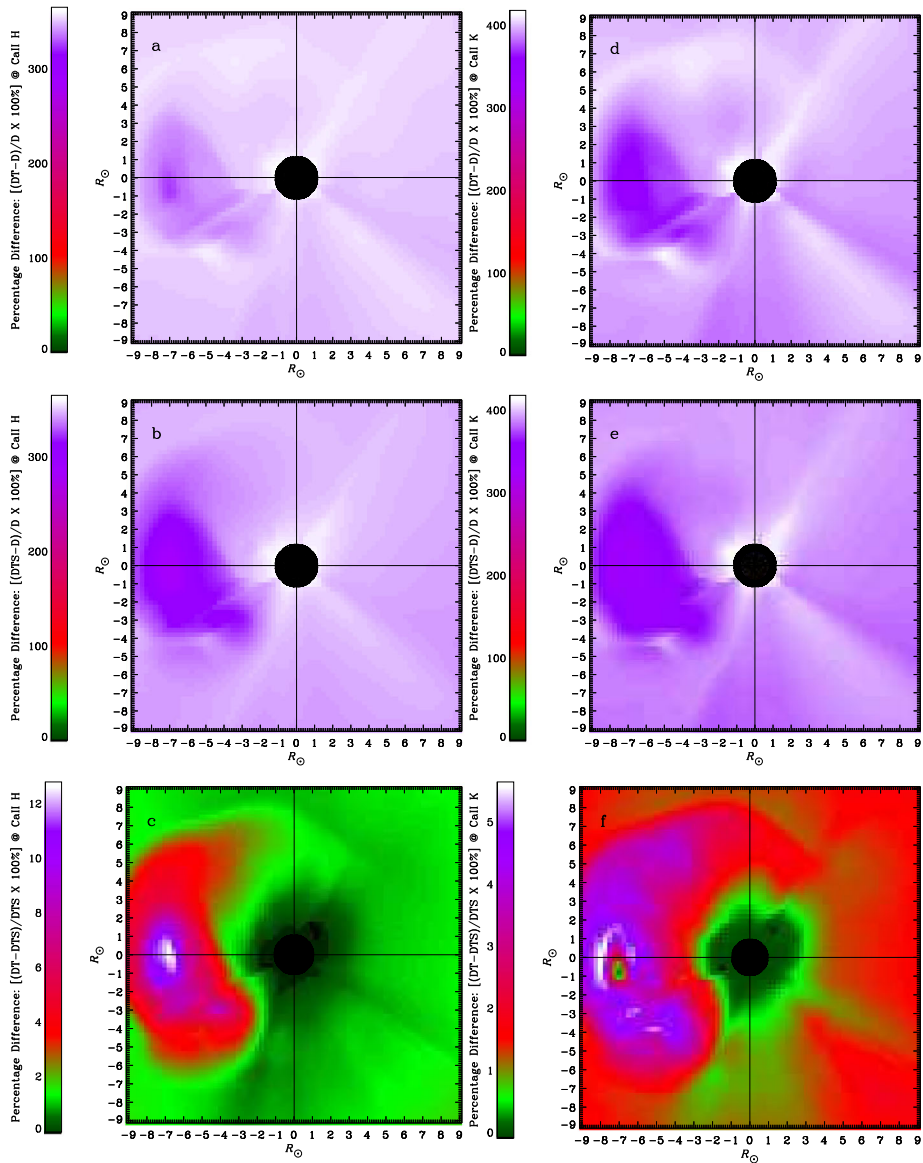


**Figure 10** Percentage differences between  $pB_{N_e}$  and  $pB_{N_e T_e}$  (a, d),  $pB_{N_e}$  and  $pB_{N_e T_e V_e}$  (b, e), and  $pB_{N_e T_e}$  and  $pB_{N_e T_e V_e}$  (c, f), where the *left column* pertains to Ca II H, and the *right column* pertains to Ca II K.

### 5. Discussion and Conclusion

To summarize, the main focus in this article is to present three important stages in the modeling of the pB spectrum over many decades, which progressively incorporated in chronological order the dependence of  $N_e$  in  $pB_{N_e}$  given by Equation 5,  $N_e$  and  $T_e$  in  $pB_{N_e T_e}$  given by Equation 6, and  $N_e$ ,  $T_e$ , and  $V_e$  in  $pB_{N_e T_e V_e}$  given by Equation 14, where  $N_e$ ,  $T_e$ , and  $V_e$  in the radial direction determine the brightness, shape, and the red-shift of the

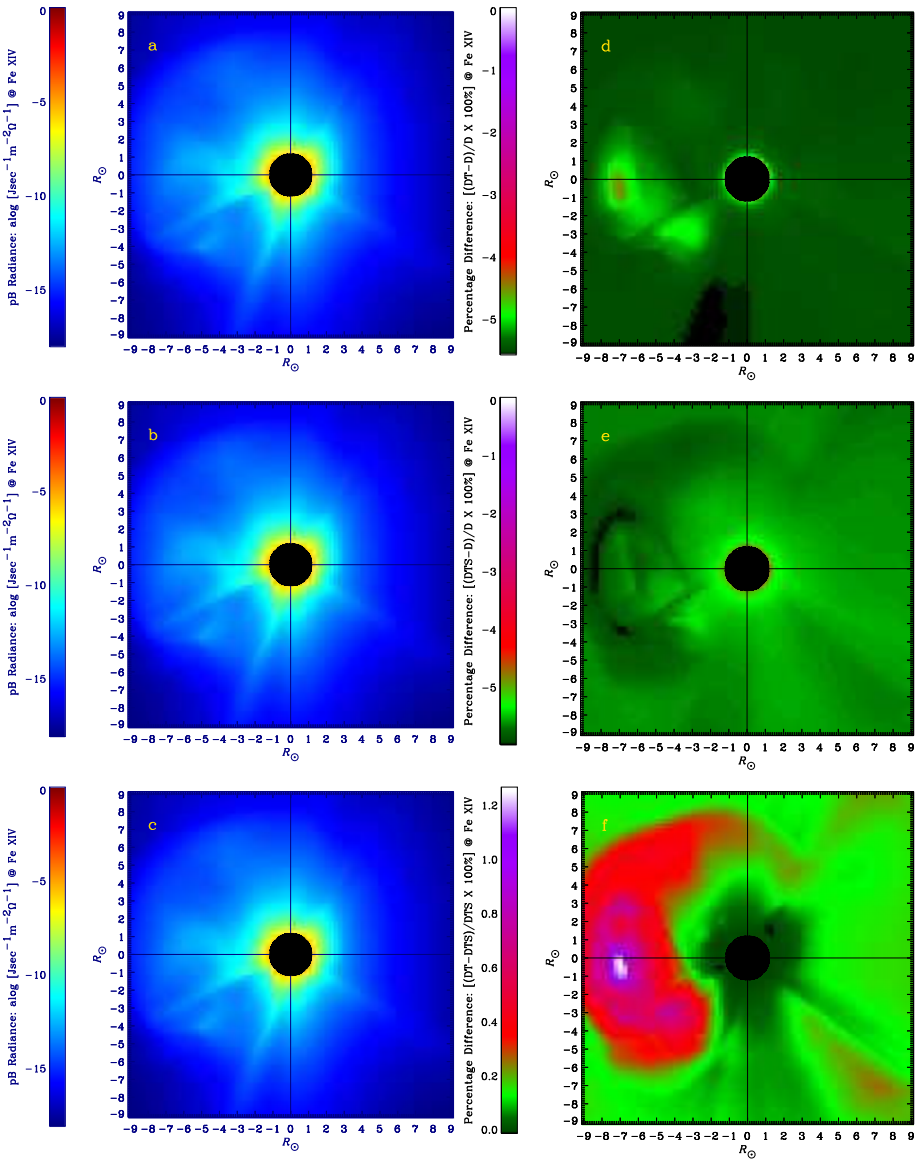


**Figure 11** Polarized K-corona brightness at 11:17:28 UT on 14 July 2004  $pB_{N_e}$  (a),  $pB_{N_eT_e}$  (b), and  $pB_{N_eT_eV_e}$  (c) corresponding to E-corona brightness of Fe xiv at  $530.3 \pm 0.3$  nm. Percentage differences between  $pB_{N_e}$  and  $pB_{N_eT_e}$  (d),  $pB_{N_e}$  and  $pB_{N_eT_eV_e}$  (e), and  $pB_{N_eT_e}$  and  $pB_{N_eT_eV_e}$  (f). Note:  $\log_e(x) = \log_{10}(x)$ .

pB spectrum, respectively. This is done to highlight the underlying physical principle of CODEX, which is designed to measure pB through multiple color filters and then match modeled  $pB_{N_eT_eV_e}$  to measure  $N_e$ ,  $T_e$ , and  $V_e$  above  $2.5 R_{\odot}$  from Sun center. To better understand the behavior of  $pB_{N_e}$ ,  $pB_{N_eT_e}$ , and  $pB_{N_eT_eV_e}$ , it is now possible to model them for select days and times using 3D model coronal environments known as Corona Heliosphere

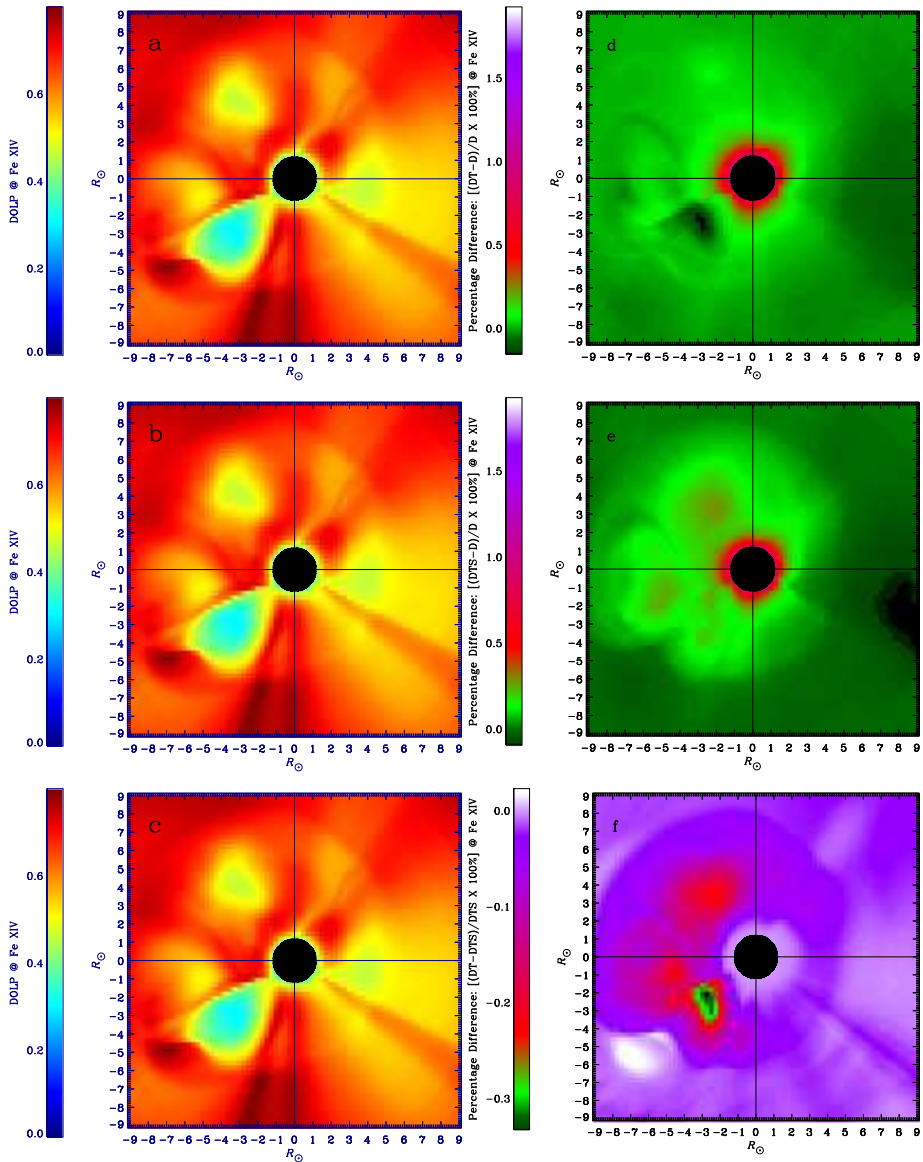


**Figure 12** DOLP at 11:17:28 UT on 14 July 2004 of  $pB_{N_e}$  (a),  $pB_{N_eT_e}$  (b), and  $pB_{N_eT_eV_e}$  (c) corresponding at E-corona brightness of Fe xiv at  $530.3 \pm 0.3$  nm. Percentage differences between  $pB_{N_e}$  and  $pB_{N_eT_e}$  (d),  $pB_{N_e}$  and  $pB_{N_eT_eV_e}$  (e), and  $pB_{N_eT_e}$  and  $pB_{N_eT_eV_e}$  (f).

(CORHEL) and Magnetohydrodynamics Around a Sphere (MAS) CORHEL–MAS models. These CORHEL–MAS models by Predictive Science Incorporated (PSI) are made available through the Community Coordinated Modeling Center (CCMC) located in NASA’s GSFC. CORHEL–MAS models are also available days prior to total solar eclipses to serve as a predictor of major coronal structures expected to be seen during totality. However, to measure  $N_e$ ,  $T_e$ , and  $V_e$ , it is not sufficient for the underlying modeled pB alone be near perfect, but it

is also equally important to measure pB as accurately as possible by paying close attention to removing unpolarized brightness from sources such as F-corona brightness, diffraction brightness, and scattering brightness, as well as polarized brightness from sources such as polarized F-corona brightness and instrumental polarization. This is because using CODEX requires matching measured pB with modeled pB. In this regard, there are challenges that need careful attention.

One such challenge to measuring pB is that the detector is illuminated not only by the K-corona brightness, which is the required signal, but also concurrently by other unwanted sources of brightness such as F-corona brightness, E-corona brightness, diffraction brightness, and stray light. As long as these unwanted sources of brightness are totally unpolarized, we expect the pB-measurement techniques mentioned in Section 2 to measure the signal. However, the unpolarized brightness will still contribute statistical noise, and some common techniques used to increase the signal-to-noise ratio (SNR) are stacking of images, which reduces temporal resolution, and binning of pixels, which reduces spatial resolution. However, in a study conducted by Lamy et al. (2020) on measuring pB using 24 years worth LASCO-C2 data from 1996 to 2019, additional data processing techniques to measure pB more accurately were presented. A very important comment made by Lamy et al. (2020) is that all the corrections proposed by them are not necessarily codified in the popular Solarsoft Library used for pB measurements of LASCO-C2 images to generate 3D reconstruction of CMEs. In light of this statement, it is prudent to study and apply if necessary the data-processing techniques presented by Lamy et al. (2020) to satisfy the need to accurately measure pB. Another challenge to measuring pB is the gradual increase in partial polarization of the F-corona brightness with coronal height. According to one estimate by Mann (1992), below 4.0 to 5.0  $R_{\odot}$  from Sun center the F-corona brightness is primarily due to diffraction of photosphere spectrum off dust and is totally unpolarized, but above 4.0 to 5.0  $R_{\odot}$  from Sun center the photosphere spectrum begins to increasingly reflect off the dust, and, as a result, F-corona brightness begins to be increasingly partially polarized with coronal height. This means that the polarization techniques discussed in Section 2 cannot prevent some fraction of the F-corona brightness mixing in with the signal and one independent way to separate them is through modeling (see Calbert and Beard, 1972, and the follow up article by Koutchmy and Magnant, 1973, who present a counternarrative to the data used by Calbert and Beard, 1972). In a study on the long-term stability of the visible F-corona brightness by Morgan and Habbal (2007), it was found to be stable between solar minimum and maximum in the range of 3.0 to 6.0  $R_{\odot}$  from Sun center, despite large changes in the shapes and activities in solar corona due to CMEs. This F-corona brightness measurements were also found to be in good agreement with the F-corona brightness measurements in the equatorial region above 5.0  $R_{\odot}$  from Sun center reported by Koutchmy and Lamy (1985), who also measured polarized F-corona brightness. For CODEX, the effects of both the polarized and unpolarized components of the F-corona brightness on the statistical noise associated with the measurements of  $T_e$  and  $V_e$  are discussed in detail by Reginald, Newmark, and Rastaetter (2021). CODEX will have an additional filter centered at 393.55 nm with a bandwidth of 1.4 nm to quantify the partially polarized F-corona brightness, and the methodology that will be used to quantify this is explained by Yang et al. (2023). An interesting event that occurs in the corona from time to time is flares that can raise  $T_e$  at localized areas to tens of mega-Kelvins. However, for the lines of sight passing through these flaring areas, their contribution toward the integrated K-corona brightness depends on  $N_e$  in those flaring areas and how they compare with  $N_e$  at the plane of sky, which will be the point on the line of sight closest to Sun center. If they are comparable, then due to the very high  $T_e$ , there is potential for even deep and conspicuous Fraunhofer lines in the SSR to be totally filled in and the hills



**Figure 13** MACS experiment conducted during the total solar eclipse of 11 August 1999 in Elazig, Turkey. The NASA team comprised of Joseph Davila (seated), Nelson Reginald (kneeling), and Charles Condor (standing). Shown in the picture is the 12-inch Schmidt–Cassegrain (SC) telescope, spectrograph (MACS), ground computer (GC) to operate the camera, field generator (FG) for power, and the fiber optic coupler (FOC) with 21 fibers between SC and MACS. The image of the totality formed on the glass surface of the FOC and the slit face of the FOC illuminated the transmission grating in MACS. The totality lasted for 124 seconds.

in the SSR totally flattened, which will make the Thomson-scattered SSR spectrum appear more like a straight line. Also, within these flaring regions, there could be very high-velocity electron streams producing significant effects on polarization rates and explained in detail by Inhester (2015). For a CODEX-type instrument, these effects will be restricted to select pixels in the detector whose lines of sight pass through these flaring regions and will need extra attention in processing and reaching conclusions.

Modeling pB additionally serves as quantifying background noise. For experiments that measure E-corona brightness, K-corona brightness is background noise. One such E-corona brightness experiment is due to the forbidden transition of Fe XIV at 530.3 nm, which is also known as the green line, can be used to measure the ion temperature and line-of-sight speed. Mierla et al. (2008) shows one such measurement using LASCO coronagraph C1, and modeled pB at 530.3 nm shown in Figure 11 is background noise, which needs to be subtracted. In another example, Habbal et al. (2021) measured the E-corona brightness of Fe XIV at 530.3 nm from the ground during a total solar eclipse to measure ion temperatures and speeds along the line of sight. Here again pB at 530.3 nm acts as a background noise that needs to be subtracted.

In conclusion, what started in the 1990s as ground-based SMT and FRT experiments to measure  $T_e$  and  $V_e$  in the radial direction during total solar eclipses that lasted a few minutes, progressed to a balloon-borne FRT experiment named the *Balloonborne Investigation of Temperature and Speed of Electrons in the Corona* (BITSE) on 18 September 2019, which lasted for  $\approx$  four hours at a height of  $\approx$  39 km in New Mexico, USA (see Gopalswamy et al., 2021), and will now evolve to a FRT experiment named CODEX on ISS in 2024 with a nominal view of the Sun for  $\approx$  45 minutes in each of its  $\approx$  90 minutes of orbit around the Earth for  $\approx$  16 orbits per day. The CODEX measurement range extends from

2.5  $R_{\odot}$  to 8.0  $R_{\odot}$  from Sun center. The data void region of CODEX from the solar limb to 2.5  $R_{\odot}$  can be measured using spare CODEX filters in a ground-based FRT experiment on 8 April 2024 when a total solar eclipse will traverse the USA and Mexico with a maximum duration of over four minutes. A spacecraft-based white-light coronagraph will continue to serve as one of the core instruments for the foreseeable future in solar coronal studies used for capturing the state of the dynamic corona. We hope that future spacecraft-based coronagraphs that will orbit the Sun with unhindered view of the Sun will be designed with FRT capabilities to produce long-term synoptic 2D maps of  $N_e$ ,  $T_e$ , and  $V_e$ . Capturing coronal images through four color filters will still show the state of the dynamic corona for traditional coronal studies of tracing coronal features and measuring  $N_e$ , which can be complemented by additionally measuring  $T_e$  and  $V_{\text{rad}}$ . Such comprehensive data sets can help in imposing crucial constraints on coronal models such as by Abbo et al. (2016), from taking multiple daily measurements to answer targeted essential questions, including: Are there signatures of hot plasma released into the solar wind from previously closed fields? What are the velocities and temperatures of the density structures that are observed so ubiquitously within streamers and coronal holes? CODEX data, both raw and processed, will be made freely available to the public.

**Acknowledgments** The authors thank the anonymous reviewer for their time in reviewing the article and for the valuable comments and suggestions. The responses to the majority of the comments were incorporated in the article, which greatly improved the clarity of the presentation. N. Reginald acknowledges that the modeling presented in Section 3 was conducted under the tutelage of Joseph Davila as his Ph.D. thesis supervisor at NASA/GSFC from January 1998 to December 2000 under a NASA Research Fellowship awarded to N. Reginald through the University of Delaware. Measuring  $pB_{N_e T_e V_e}$  followed the modeling with N. Reginald designing and assembling the *Multi Aperture Coronal Spectrograph* (MACS), as shown in Figure 13, to simultaneously measure both  $T_e$  and  $V_e$  during the total solar eclipse of 11 August 1999 in Elazig, Turkey. N. Reginald also acknowledges support by NASA Goddard Space Flight Center through Cooperative Agreement 80NSSC21M0180 to The Catholic University of America, Partnership for Heliophysics and Space Environment Research (PHaSER). We thank PSI for sharing the Bastille Day coronal model data made available through the CCMC at NASA-GSFC that allowed us to carry out the computations in Section 4.

**Author contributions** N. Reginald: Wrote the IDL codes for the three polarized brightness models in Section 3 and created all the figures. L. Rastaetter: Wrote the IDL code to read the electron density, temperature, and radial velocity data along lines of sight passing through the Bastille Day CME model that were used as inputs in the three polarized brightness model spectra to generate the associated polarized brightness maps in Section 4. J. Newmark: Provided the overall structure of the manuscript for the benefit of readers who would want to better understand CODEX. J. Newmark is the PI of CODEX. All the authors reviewed the manuscript.

## Declarations

**Competing interests** The authors declare no competing interests.

## References

- Abbo, L., Ofman, L., Antiochos, S.K., Hansteen, V.H., Harra, L., Ko, Y.K., Lapenta, G., Li, B., Riley, P., Strachan, L., von Steiger, R., Wang, Y.M.: 2016, Slow solar wind: observations and modeling. *Space Sci. Rev.* **201**, 55. DOI. ADS.
- Altschuler, M.D., Newkirk, G.: 1969, Magnetic Fields and the Structure of the Solar Corona. I: Methods of Calculating Coronal Fields. *Solar Phys.* **9**, 131. DOI. ADS.
- Baumbach, S.: 1937, Strahlung, Ergiebigkeit und Electronendichte der Sonnenkorona. *Astron. Nachr.* **263**, 121. DOI.
- Baumbach, S.: 1938, Die Polarisation der Sonnenkorona. *Astron. Nachr.* **267**, 273. DOI.
- Billings, D.E.: 1966, *A Guide to the Solar Corona*, Academic Press, New York.

- Brueckner, G.E., Howard, R.A., Koomen, M.J., Korendyke, C.M., Michels, D.J., Moses, J.D., Socker, D.G., Dere, K.P., Lamy, P.L., Llebaria, A., Bout, M.V., Schwenn, R., Simnett, G.M., Bedford, D.K., Eyles, C.J.: 1995, The Large Angle Spectroscopic Coronagraph (LASCO). *Solar Phys.* **162**, 357. DOI ADS.
- Calbert, R., Beard, D.B.: 1972, The F and K components of the solar corona. *Astrophys. J.* **176**, 497. DOI ADS.
- Cram, L.E.: 1976, Determination of the temperature of the solar corona from the spectrum of the electron-scattering continuum. *Solar Phys.* **48**, 3. DOI ADS.
- Gibson, S.E., Foster, D., Burkepile, J., de Toma, G., Stanger, A.: 2006, The calm before the storm: the link between quiescent cavities and coronal mass ejections. *Astrophys. J.* **641**, 590. DOI ADS.
- Gopalswamy, N., Newmark, J., Yashiro, S., Mäkelä, C.M., Michels, P., Reginald, N., Thakur, N., Gong, Q., Kim, Y.H., Cho, K.S., Choi, S.H., Baek, J.H., Bong, S.C., Yang, H.S., Park, J.Y., Lee, J.O., Kim, R.S., Lim, E.K.: 2021, The balloon-borne investigation of temperature and speed of electrons in the corona (BITSE): mission description and preliminary results. *Solar Phys.* **296**, 15. DOI ADS.
- Grotirio, W.: 1931, Ergebnisse der Potsdamer Expedition zur Beobachtung der Sonnenfinsternis am 9. Mai 1929 in Takengon (Nordsumatra). 6. Mitteilung. Über die Intensitätsverteilung des kontinuierlichen Spektrums der inneren Korona. Mit 8 Abbildungen. (Eingegangen am 27. Juni 1931). *Z. Astrophys.* **3**, 199. ADS.
- Guhathahurta, M., Holzer, T.E., MacQueen, R.M.: 1996, The large-scale density structure of the solar corona and the heliospheric current sheet. *Astrophys. J.* **458**, 817. DOI ADS.
- Habbal, S.R., Druckmüller, M., Alzate, N., Ding, A., Johnson, J., Starha, P., Hoderova, J., Boe, B., Constantinou, S., Amdt, M.: 2021, Identifying the coronal source regions of solar wind streams from total solar eclipse observations and in situ measurements extending over a solar cycle. *Astrophys. J. Lett.* **911**, 12. DOI ADS.
- Harder, J., Bèland, S., Pentan, S.V., Richard, E., Weatherhead, E., Araujo-Pradere, E.: 2022, SORCE and TSIS-1 SIM comparison: absolute irradiance scale reconciliation. *Earth Space Sci.* **9**, 3e20122. DOI ADS.
- Hoeksema, J.T.: 1984, Structure and Evolution of the Large Scale Solar and Heliospheric Magnetic Fields. Ph.D. thesis, Stanford University. ADS.
- Howard, R.A., Moses, J.D., Vourlidas, A., Newmark, J.S., Socker, D.G., Plunkett, S.P., Korendyke, C.M., Cook, J.W., Hurley, A., Davila, J.M., Thompson, W.T., St Cyr, O.C., Mentzell, E., Mehalick, K., Lemen, J.R., Wuelsel, J.P., Duncan, D.W., Tarbell, T.D., Wolfson, C.J., Moore, A., Harrison, R.A., Waltham, N.R., Lang, J., Davis, C.J., Eyles, C.J., Mapson-Menard, H., Simnett, G.M., Halain, J.P., Defise, J.M., Mazy, E., Rochus, P., Mercier, R., Ravet, M.F., Delmotte, F., Auchère, F., Delaboudinière, J.P., Bothmer, V., Deutsch, W., Wang, D., Rich, N., Cooper, S., Stephens, V., Maahs, G., Baugh, R., McMullin, D., Carter, T.: 2008, Sun Earth connection coronal and heliospheric investigation (SECCHI). *Space Sci. Rev.* **136**, 67. DOI ADS.
- Hundhausen, A.J.: 1993, Sizes and loactions of coronal mass ejections: SMM observations from 1980 and 1984–1989. *J. Geophys. Res.* **98**, 13177. DOI ADS.
- Ichimoto, K., Kumagai, K., Sano, I., Kobiki, T., Sakurai, T.: 1996, Measurement of the coronal electron temperature at the total solar eclipse on 1994 November 3. *Publ. Astron. Soc. Japan* **48**, 545. DOI ADS.
- Inhester, B.: 2015, Thomson Scattering in the Solar Corona. ArXiv e-prints DOI.
- Kim, I.S., Nasonova, L.P., Lisin, D.V., Popov, V.V., Krusanova, N.L.: 2017, Imaging the structure of the low K-corona. *J. Geophys. Res.* **122**, 77. DOI ADS.
- Koutchmy, S., Lamy, P.L.: 1985, The F-corona and the circum-solar dust evidences and properties [G. Nikolasky memorial lecture]. In: Giese, R.H., Lamy, P. (eds.), *Properties and Interactions of Interplanetary Dust, IAU Colloq. 85, Astrophys. Space Sci. Lib.* **119**, 63. Reidel, Dordrecht. DOI ADS.
- Koutchmy, S., Magnant, F.: 1973, On the observation of the F-corona in the vicinity of the solar limb. *Astrophys. J.* **186**, 671. DOI ADS.
- Kurucz, R.L., Furenlid, N., Brault, J., Testerman, L.: 1984, Solar flux atlas from 296 nm 1300 nm. Tucson, National Solar Observatory.
- Lamy, P., Llebaria, A., Boclet, B., Gilardy, H., Burtin, M., Floyd, O., 2020, Coronal photopolarimetry with the LASCO-C2 coronagraph over 24 years [1996–2019]. *Solar Phys.* **183**, 165. DOI ADS.
- Leblanc, Y., Dulk, G.A., Bougeret, J.L.: 1998, Tracing the electron density from the corona to 1au. *Solar Phys.* **183**, 165. DOI ADS.
- Mann, I.: 1992, The solar F-corona: calculations of the optical and infrared brightness of circumstellar dust. *Astron. Astrophys.* **261**, 329. ADS.
- Mierla, M., Schwenn, R., Teriaca, L., Stenborg, G., Podlipnik, B.: 2008, Analysis of the Fe X and Fe XIV line width in the solar corona using LASCO-C1 spectral data. *Astron. Astrophys.* **480**, 509. DOI ADS.
- Minnnaert, M.: 1930, On the continuous spectrum of the corona and its polarization. *Z. Astrophys.* **1**, 209. ADS.

- Morgan, H.: 2015, An atlas of coronal electron density at 5  $R_{\odot}$ . I. Data processing and calibration. *Astron. Astrophys. Suppl. Ser.* **219**, 23. DOI. ADS.
- Morgan, H., Habbal, S.: 2007, The long-term stability of the visible F-corona at heights of 3–6  $R_{\odot}$ . *Astron. Astrophys.* **471**, L47. DOI. ADS.
- November, L.J., Koutchmy, S.: 1996, White-light coronal dark threads and density fine structure. *Astrophys. J.* **466**, 512. DOI. ADS.
- Reginald, N.L.: 2001, MACS, an instrument, and a methodology for simultaneous and global measurements of the coronal electron temperature and the solar wind velocity on the solar corona. Ph.D. thesis, Univ. Delaware. ADS.
- Reginald, N.L., Davila, J.M.: 2000, MACS for global measurement of the solar wind velocity and the thermal electron temperature during the total solar eclipse on 11 August 1999. *Solar Phys.* **195**, 111. DOI. ADS.
- Reginald, N.L., Davila, J.M., St. Cyr, O.C.: 2004, The effects of streamers on the shape of the K-coronal spectrum. *Solar Phys.* **225**, 249. DOI. ADS.
- Reginald, N.L., Newmark, J., Rastaetter, L.: 2019, Measuring electron temperature using a linear polarizer versus a polarization camera. *Solar Phys.* **294**, 100. DOI. ADS.
- Reginald, N.L., Newmark, J., Rastaetter, L.: 2020, Synoptic measurements of electron temperature and speed in the solar corona with next generation white-light coronagraph. *Solar Phys.* **295**, 95. DOI. ADS.
- Reginald, N.L., Newmark, J., Rastaetter, L.: 2021, Statistical error analysis on white-light filter ratio experiments to measure electron parameters. *Solar Phys.* **196**, 146. DOI. ADS.
- Reginald, N.L., Rastaetter, L.: 2019, Dependence of DOLP on coronal electron temperature, speed, and structure. *Solar Phys.* **294**, 12. DOI. ADS.
- Reginald, N.L., St. Cyr, O.C., Davila, J.M., Brosius, J.W.: 2003, Electron temperature and speed measurements in the low solar corona: results from the 2001 June eclipse. *Astrophys. J.* **599**, 596. DOI. ADS.
- Reginald, N.L., St. Cyr, O.C., Davila, J.M., Guhathakurta, M., Hassler, D.M.: 2009, Electron-temperature maps of the low solar corona. ISCORE results from the total solar eclipse of 21 June 2006 in Libya. *Solar Phys.* **270**, 235. DOI. ADS.
- Reginald, N.L., Davila, J.M., St. Cyr, O.C., Rabin, D.M., Guhathakurta, M., Hassler, D.M., Gashut, H.: 2011, Electron temperature and flow speed of the low solar corona measurement. MACS results from the total solar eclipse of 21 June 2006 in Libya. *Solar Phys.* **270**, 235. DOI. ADS.
- Reginald, N.L., Gopalswamy, N., Yashiro, S., Gong, Q., Guhathakurta, M.: 2017, Replacing the polarizer wheel with a polarization camera to increase the temporal resolution and to reduce the overall complexity of a solar coronagraph. *J. Astron. Telesc. Instrum. Syst.* **3**, 014001. DOI. ADS.
- Reginald, N.L., Newmark, J., Rastaetter, L., Török, T.: 2018, Evaluating uncertainties in coronal electron temperature and radial speed measurement using a simulation of the Bastille Day eruption. *Solar Phys.* **293**, 82. DOI. ADS.
- Saito, K., Poland, A.I., Munro, R.H.: 1977, A study of the background corona near solar minimum. *Solar Phys.* **55**, 121. DOI. ADS.
- Saito, K., Makita, M., Nishi, K., Hata, S.: 1977, A non-spherical axisymmetric model of the solar K corona of the minimum type. *Ann. Tokyo Astron. Obs.* **12**, 51. ADS.
- Schatten, K.H., Wilcox, J.M., Ness, N.F.: 1969, A model of interplanetary and coronal magnetic fields. *Solar Phys.* **6**, 442. DOI. ADS.
- Schuster, A.: 1879, On the polarization of the solar corona. *Mon. Not. Roy. Astron. Soc.* **40**, 35. ADS.
- Shklovskii, I.S.: 1965, *Physics of the Solar Corona*, Pergamon, Oxford.
- Török, T., Downes, C., Linker, J.A., Lionello, R., Titov, V.S., Mikić, Z., Riley, P., Caplan, R.M., Wijaya, J.: 2018, Sun-to-Earth MHD simulation of the 2000 July 14 Bastille Day Eruption. *Astrophys. J.* **856**, 75. DOI. ADS.
- Van de Hulst, H.C.: 1950, The electron density of the solar corona. *Bull. Astron. Inst. Neth.* **11**, 135. ADS.
- van Houten, C.J.: 1950, The form of Fraunhofer lines in the inner corona. *Bull. Astron. Inst. Neth.* **11**, 160. ADS.
- Wang, T., Reginald, N.L., Davila, J.M., St. Cyr, O.C., Thompson, W.T.: 2017, Variation in coronal activity from solar cycle 24 minimum to maximum using three-dimensional reconstructions of the coronal electron density from STEREO/COR1. *Solar Phys.* **292**, 97. DOI. ADS.
- Woltjer, J.: 1926, On the continuous spectrum of the corona. *Bull. Astron. Inst. Neth.* **3**, 103. ADS.
- Woltjer, J.: 1926, Additional note on the continuous spectrum of the corona. *Bull. Astron. Inst. Neth.* **3**, 163. ADS.
- Yang, H., Cho, S., Bong, O.C., Madjarska, M.S., Kim, Y., Reginald, N., Newmark, J.M.: 2023, Feasibility study of measuring degree of linear polarization of the solar F-corona using filter observations on the COroanal diagnostic EXperiment. *Solar Phys.* **298**, 57. DOI. ADS.

**Publisher's Note** Springer Nature remains neutral with regard to jurisdictional claims in published maps and institutional affiliations.

Springer Nature or its licensor (e.g. a society or other partner) holds exclusive rights to this article under a publishing agreement with the author(s) or other rightsholder(s); author self-archiving of the accepted manuscript version of this article is solely governed by the terms of such publishing agreement and applicable law.